



A stable and accurate immersed boundary method for simulating vesicle dynamics via spherical harmonics

Ming-Chih Lai^a, Yunchang Seol^{b,*}

^a Department of Applied Mathematics, National Yang Ming Chiao Tung University, 1001 Ta Hsueh Road, Hsinchu 30010, Taiwan

^b Department of Mathematics, Kyungpook National University, Daegu 41566, Republic of Korea



ARTICLE INFO

Article history:

Available online 18 October 2021

Keywords:

Vesicle
Immersed boundary method
Spherical harmonics
Viscosity contrast
Inertia effect
Mesh control

ABSTRACT

In this paper, we improve our previous immersed boundary (IB) method for 3D triangulated vesicle in unsteady Navier-Stokes flow (Seol et al., 2016 [31]) from several aspects. Firstly, we adopt spherical harmonic representation for approximating vesicle configuration. By applying spectral differentiation, we are able to obtain high accuracy of geometric quantities such as the mean and Gaussian curvatures, and the surface Laplacian of mean curvature, which is not achievable via triangulation. The vesicle membrane (interface) immersed in 3D Newtonian fluid ensures the surface incompressibility constraint; thus, an unknown elastic tension acting as Lagrange multiplier must be introduced along the interface. To efficiently solve the problem, a logarithmic formulation of approximate elastic tension is explicitly utilized in a nearly incompressible interface approach. Then in computing the elastic tension force, we propose to use the divergence form instead of the commonly used non-divergence one. By doing so, we find that numerical stability can be improved significantly during vesicle relaxation and its transient motions. Moreover, to maintain the interfacial mesh quality, a mesh control technique via filtering of interfacial tangential velocity is coupled within the nearly incompressible interface approach. Upon these improvements, a series of numerical tests on the present scheme is performed to verify numerical accuracy, stability, and convergence of our method. As for practical experiments, the tank-treading and tumbling motions of prolate vesicle in shear flow are extensively studied by varying some dimensionless parameters such as the reduced volume, bending capillary number, viscosity contrast, and the Reynolds number. We further study three types of vesicle shapes, namely, bullet, parachute, and croissant in rectangular Poiseuille flow.

© 2021 Elsevier Inc. All rights reserved.

1. Introduction

A vesicle behaves like fluidic droplet enclosed by a phospholipid membrane immersed in a viscous incompressible fluid. The underlying dynamics are determined by the membrane bending resistance, interfacial incompressibility, and non-local hydrodynamic forces. The vesicle shares similar behaviors with the red blood cell (RBC), so its importance has received a great deal of attention since it can be used for various experimental purposes [25]. Some practical applications of vesicle in bioengineering include a micro-reactor [10] and a drug-delivery vehicle [32].

* Corresponding author.

E-mail addresses: mclai@math.nctu.edu.tw (M.-C. Lai), ycseol@knu.ac.kr (Y. Seol).

A typical vesicle radius is about 10 μm which presumes the Stokes regime of vesicle dynamics. Its tank-treading and tumbling motions have been studied in Stokes flow extensively. For this, the boundary integral method (BIM) is widely used as in [22,39,40,47,4,9], since the fluid velocity via Green's function satisfies the fluid incompressibility automatically. The interfacial incompressibility as an extra constraint can be further imposed by solving the unknown elastic tension.

In the human blood circulatory system, especially in normal arterioles, the Reynolds number of blood flow may be higher than one, see [28] and references therein for a review of hemorheology. The experimental observation indicates that the fluid flow surrounding vesicles (as a prototype of RBCs) can occur in the Navier-Stokes regime, thereby the inertia effect may give rise to transient motion of vesicle even when the Reynolds number is $O(1)$. Thus, in order to study the vesicle dynamics including inertia effect, several numerical approaches have been developed, such as immersed boundary or front-tracking method [19,20,45,31,26], level-set method [29,21], diffuse interface or phase-field method [7,3,1], finite element method [2], lattice Boltzmann method [13,11,16], and hybrid method [23], just to name a few. In all of these methods above, a challenging issue is the simultaneous satisfaction of two local constraints; namely, the fluid and interfacial incompressibilities. To resolve this issue effectively, the present authors introduced a nearly incompressible interface in [31] within the 3D immersed boundary framework [27], refer to similar approach in [45]. Other than this approach, a special algorithm shall be devised to enforce both incompressibilities, which requires to solve the whole fluid system with unknown elastic tension via iterative methods.

In this paper, we propose a stable and accurate method for solving the quasi-spherical vesicle motion in Navier-Stokes flow. The present method improves the prior work on triangulated nearly incompressible vesicle [31] in four aspects as follows.

- Firstly, the vesicle interface is discretized in spherical coordinates, enabling to employ spherical harmonic expansion for spectral approximation. By doing so, high accuracy of discrete geometric quantities can be obtained, in particular the bending force is accurately computed via spectral differentiation coupled with upsampling algorithm.
- Secondly, the logarithmic formulation of approximate elastic tension is explicitly utilized to conserve local surface area. Compared to linear formulation used in [31], the logarithmic formulation written in Eq. (5) gives larger feedback force when local surface area decreases, preventing ideally the clustering of Lagrangian markers around two poles in spherical coordinates. As derived in [24], the corresponding tension force has interestingly the same form as the original one subject to the logarithmic definition of elastic tension.
- Thirdly, to compute elastic tension force in Eq. (6), we employ the divergence form $\nabla_{\Gamma} \cdot (\sigma \mathbb{P})$, instead of the commonly used non-divergence form $\nabla_{\Gamma} \sigma - 2\sigma H \mathbf{n}$. We find that the divergence form improves the numerical stability of evolving vesicle shapes. From a simple error estimation, we attribute the numerical instability to the imbalance of tangential and normal components of elastic tension force by using non-divergence form. To clarify this point, some convincing numerical evidences are provided as well.
- Lastly, the mesh control of vesicle interface via filtering of tangential velocity is combined within the framework of spherical harmonic expansion. The present mesh control technique not only stabilizes the computation but also keeps the local surface area well in the nearly incompressible interface approach.

Generally speaking, all above improvements are essential to accurately accomplish and stably sustain the evolving vesicle configured in spherical coordinates under various dynamic flows.

The rest of this paper is organized as follows. In next section, we present the governing equations based on the immersed boundary framework, which describe a nearly incompressible vesicle dynamics in unsteady Navier-Stokes flow. Some related surface differential operators and geometric quantities are also introduced. In Section 3, the dimensionless governing equations are presented together with their numerical discretizations. Besides, spectral differentiations up to second-order via spherical harmonic transform are presented to compute the needed discrete surface quantities. An upsampling algorithm for surface Laplacian of mean curvature is also introduced. In Section 4, we begin with numerical accuracy check for geometric quantities associated with the bending force. Then in computing elastic tension force, the improved numerical stability by using the divergence form is studied in comparison with the non-divergence form. After studying the convergence behavior of relaxing vesicle under quiescent flow, a series of numerical experiments under shear flow are performed to show the applicability of our method. Thereby, the effects of the dimensionless parameters such as the reduced volume, bending capillary number, viscosity contrast, and the Reynolds number are extensively investigated. Vesicle motions in Poiseuille flow are also studied. Some conclusions are given in Section 5.

2. Mathematical model

In this paper, we consider fluidic vesicle dynamics in three-dimensional incompressible fluid domain Ω . The interface Γ of vesicle separating two fluids is assumed to be a smooth surface immersed in Ω . The model is formulated by the immersed boundary method in which the elastic tension force \mathbf{F}_{σ} , the bending force \mathbf{F}_b , and the volume conservation force \mathbf{F}_v are imposed along the vesicle interface. (Note that, here we add the extra \mathbf{F}_v term simply for numerical purpose.) The fluid velocity $\mathbf{u}(\mathbf{x}, t)$ and pressure $p(\mathbf{x}, t)$ are described in Eulerian manner while the interface $\mathbf{X}(\alpha, \beta, t)$ and the elastic tension $\sigma(\alpha, \beta, t)$ are described in Lagrangian manner, so the governing equations of this vesicle model can be written in a single fluid system as follows.

$$\rho \left(\frac{\partial \mathbf{u}}{\partial t} + (\mathbf{u} \cdot \nabla) \mathbf{u} \right) = -\nabla p + \nabla \cdot [(\mu_o + I(\mu_i - \mu_o)) (\nabla \mathbf{u} + \nabla \mathbf{u}^T)] + \mathbf{f} \quad \text{in } \Omega, \quad (1)$$

$$\nabla \cdot \mathbf{u} = 0 \quad \text{in } \Omega, \quad (2)$$

$$\mathbf{f}(\mathbf{x}, t) = \int_{\Gamma} (\mathbf{F}_\sigma + \mathbf{F}_b + \mathbf{F}_v) \delta(\mathbf{x} - \mathbf{X}(\alpha, \beta, t)) dA \quad \text{in } \Omega, \quad (3)$$

$$\frac{\partial \mathbf{X}}{\partial t}(\alpha, \beta, t) := \mathbf{U}(\alpha, \beta, t) = \int_{\Omega} \mathbf{u}(\mathbf{x}, t) \delta(\mathbf{x} - \mathbf{X}(\alpha, \beta, t)) d\mathbf{x} \quad \text{on } \Gamma, \quad (4)$$

$$\sigma(\alpha, \beta, t) = \sigma_0 \left(\frac{|\mathbf{X}_\alpha^0 \times \mathbf{X}_\beta^0|}{|\mathbf{X}_\alpha \times \mathbf{X}_\beta|} \right) \ln \left(\frac{|\mathbf{X}_\alpha \times \mathbf{X}_\beta|}{|\mathbf{X}_\alpha^0 \times \mathbf{X}_\beta^0|} \right) \quad \text{on } \Gamma, \quad (5)$$

$$\mathbf{F}_\sigma(\alpha, \beta, t) = \nabla_\Gamma \cdot (\sigma \mathbb{P}) = \nabla_\Gamma \sigma - 2\sigma H \mathbf{n} \quad \text{on } \Gamma, \quad (6)$$

$$\mathbf{F}_b(\alpha, \beta, t) = \frac{c_b}{2} [\Delta_\Gamma H + 2H(H^2 - K)] \mathbf{n} \quad \text{on } \Gamma, \quad (7)$$

$$\mathbf{F}_v(\alpha, \beta, t) = -c_v \left(\frac{V(t) - V(0)}{V(0)} \right) \mathbf{n} \quad \text{on } \Gamma, \quad (8)$$

where

$$\mathbb{P} = \mathbb{I} - \mathbf{n}\mathbf{n}^T, \quad \mathbf{n} = \frac{\mathbf{X}_\alpha \times \mathbf{X}_\beta}{|\mathbf{X}_\alpha \times \mathbf{X}_\beta|} := (n_1, n_2, n_3). \quad (9)$$

Eqs. (1) and (2) are the Navier-Stokes equations and we assume herein that the fluid has a constant density ρ . The fluid viscosity μ can be different between two fluids as we use $\mu = \mu_o + I(\mu_i - \mu_o)$ above. Here μ_i and μ_o are the associated constant viscosities of inner and outer fluids of vesicle satisfying $\mu_i \geq \mu_o$, and I is the indicator (or Heaviside) function defined by

$$I(\mathbf{x}, t) = \begin{cases} 1 & \text{if } \mathbf{x} \text{ is inside the vesicle interface,} \\ 0 & \text{otherwise.} \end{cases}$$

In Eq. (3), the Eulerian force \mathbf{f} arises from the spreading of interfacial force via the Dirac delta function $\delta(\mathbf{x}) = \delta(x)\delta(y)\delta(z)$. Similarly, as shown in Eq. (4), the interfacial velocity \mathbf{U} is interpolated from the local Eulerian fluid velocity via the delta function.

In traditional vesicle problem, enforcing the exact incompressible interface condition $\nabla_\Gamma \cdot \mathbf{U} = 0$ involves solving the unknown elastic tension σ , which acts as Lagrange multiplier of the condition. In the present model, the interfacial incompressibility is alternatively approximated without finding σ by a nearly incompressible interface approach as in [31]. However, unlike a linear spring-like tension used in [31], we use a logarithmic form of tension (5) derived in [24] by the present authors which not only has the effect of keeping the local surface area conserved but also has the advantage of preventing the clustering of markers at two poles in spherical coordinates. The logarithmic approach is based on the formula

$$\frac{\partial}{\partial t} (\ln |\mathbf{X}_\alpha \times \mathbf{X}_\beta|) = \nabla_\Gamma \cdot \mathbf{U}.$$

Thus, to enforce $\ln(|\mathbf{X}_\alpha \times \mathbf{X}_\beta|) - \ln(|\mathbf{X}_\alpha^0 \times \mathbf{X}_\beta^0|) = \ln \frac{|\mathbf{X}_\alpha \times \mathbf{X}_\beta|}{|\mathbf{X}_\alpha^0 \times \mathbf{X}_\beta^0|} \approx 0$ is equivalent to the constraint $\nabla_\Gamma \cdot \mathbf{U} \approx 0$, where $|\mathbf{X}_\alpha \times \mathbf{X}_\beta|$ and $|\mathbf{X}_\alpha^0 \times \mathbf{X}_\beta^0|$ are the respective stretching factors at time t and initial time. The tension written in Eq. (5) is derived by taking the first variation of

$$E_\sigma = \frac{\sigma_0}{2} \iint \left[\ln \left(\frac{|\mathbf{X}_\alpha \times \mathbf{X}_\beta|}{|\mathbf{X}_\alpha^0 \times \mathbf{X}_\beta^0|} \right) \right]^2 |\mathbf{X}_\alpha^0 \times \mathbf{X}_\beta^0| d\alpha d\beta,$$

from which it is surprising to recover the original form of tension force as written in Eq. (6) but with the logarithmic definition of approximate elastic tension. That is, we have $\mathbf{F}_\sigma = -\frac{\delta E_\sigma}{\delta \mathbf{X}}$, where σ has the form of Eq. (5).

Using the above nearly incompressible interface approach, the elastic tension force \mathbf{F}_σ in Eq. (6) is no longer an unknown function and can be computed through the interface configuration \mathbf{X} . To compute the tension force explicitly, there are two formulas as written in Eq. (6); one is the divergence form $\nabla_\Gamma \cdot (\sigma \mathbb{P})$, and the other is the non-divergence form $\nabla_\Gamma \sigma - 2\sigma H \mathbf{n}$. For a smooth surface Γ , the two forms are equivalent as derived in the following:

$$\begin{aligned}
 & \nabla_\Gamma \cdot (\sigma \mathbb{P}) \\
 &= (\nabla_\Gamma \sigma) \mathbb{P} + \sigma \nabla_\Gamma \cdot \mathbb{P} \\
 &= \nabla_\Gamma \sigma - \sigma \nabla_\Gamma \cdot (\mathbf{n} \mathbf{n}^T) \quad (\text{by } \mathbf{u} \mathbb{P} = \mathbf{u} \text{ for tangent vector } \mathbf{u} \text{ and } \nabla_\Gamma \cdot \mathbb{I} = 0) \\
 &= \nabla_\Gamma \sigma - \sigma (\mathbf{n} \nabla_\Gamma \cdot \mathbf{n} + \mathbf{n} \cdot \nabla_\Gamma \mathbf{n}) \quad (\text{by } \nabla_\Gamma \cdot (n_i \mathbf{n}) = n_i \nabla_\Gamma \cdot \mathbf{n} + \mathbf{n} \cdot \nabla_\Gamma n_i) \\
 &= \nabla_\Gamma \sigma - 2\sigma H \mathbf{n} \quad (\text{by } \nabla_\Gamma \cdot \mathbf{n} = 2H \text{ and } \mathbf{n} \cdot \nabla_\Gamma n_i = 0).
 \end{aligned}$$

It is common to compute the non-divergence form of discrete elastic tension force in literature [40,31,33]; however, we propose to use the divergence form due to improved numerical stability as we can see some compelling numerical advantages later in Subsection 4.2.

The bending force \mathbf{F}_b in Eq. (7) resists interfacial bending of vesicle, where H and K are the mean and Gaussian curvatures, respectively, and $\Delta_\Gamma H$ is the surface Laplacian of H . This force can be derived from the Willmore [42] (or Canham-Helfrich bending [15]) energy functional $E_b = \frac{c_b}{2} \int_\Gamma H^2 dA$. The penalty force (as a feedback mechanism) for volume conservation is given in Eq. (8), where c_v is the penalty parameter and $V(t)$ is the enclosed volume of vesicle at time t . In Eq. (9), the projection operator \mathbb{P} is defined by the 3-by-3 identity matrix \mathbb{I} and the outward unit normal vector \mathbf{n} . To solve the governing equations (1)-(8), one shall impose adequate initial and boundary conditions.

For the sake of completeness, we write down the precise formulas of surface gradient operator ∇_Γ and the surface divergence operator $\nabla_\Gamma \cdot$ used in this paper. For a surface patch $\mathbf{X}(\alpha, \beta)$ at a fixed time (the time variable t is omitted), the coefficients of the first and second fundamental forms are defined by

$$E = \mathbf{X}_\alpha \cdot \mathbf{X}_\alpha, \quad F = \mathbf{X}_\alpha \cdot \mathbf{X}_\beta, \quad G = \mathbf{X}_\beta \cdot \mathbf{X}_\beta, \quad L = \mathbf{X}_{\alpha\alpha} \cdot \mathbf{n}, \quad M = \mathbf{X}_{\alpha\beta} \cdot \mathbf{n}, \quad N = \mathbf{X}_{\beta\beta} \cdot \mathbf{n},$$

where the subscripts α and β of a function denote its partial derivatives with respect to α and β , respectively. So the mean and Gaussian curvatures of the surface are obtained by

$$H = \frac{-GL - EN + 2FM}{2(EG - F^2)}, \quad K = \frac{LN - M^2}{EG - F^2}. \tag{10}$$

With these notations, the surface gradient operator of a scalar function $\sigma(\alpha, \beta)$ is represented by

$$\nabla_\Gamma \sigma = \frac{G\sigma_\alpha - F\sigma_\beta}{EG - F^2} \mathbf{X}_\alpha + \frac{E\sigma_\beta - F\sigma_\alpha}{EG - F^2} \mathbf{X}_\beta, \tag{11}$$

and similarly, the surface divergence operator of a vector field $\mathbf{U}(\alpha, \beta)$ is

$$\nabla_\Gamma \cdot \mathbf{U} = \frac{G\mathbf{U}_\alpha - F\mathbf{U}_\beta}{EG - F^2} \cdot \mathbf{X}_\alpha + \frac{E\mathbf{U}_\beta - F\mathbf{U}_\alpha}{EG - F^2} \cdot \mathbf{X}_\beta. \tag{12}$$

For a tangent vector of the form $\mathbf{V} = P(\alpha, \beta)\mathbf{X}_\alpha + Q(\alpha, \beta)\mathbf{X}_\beta$, an alternative of the surface divergence operator can be written by

$$\nabla_\Gamma \cdot \mathbf{V} = \frac{1}{\sqrt{EG - F^2}} \left[\left(P\sqrt{EG - F^2} \right)_\alpha + \left(Q\sqrt{EG - F^2} \right)_\beta \right], \tag{13}$$

hence the surface Laplacian of mean curvature function $H(\alpha, \beta)$ is written by

$$\Delta_\Gamma H := \nabla_\Gamma \cdot \nabla_\Gamma H = \frac{1}{\sqrt{EG - F^2}} \left[\left(\frac{GH_\alpha - FH_\beta}{\sqrt{EG - F^2}} \right)_\alpha + \left(\frac{EH_\beta - FH_\alpha}{\sqrt{EG - F^2}} \right)_\beta \right]. \tag{14}$$

The surface stretching element is given by $|\mathbf{X}_\alpha \times \mathbf{X}_\beta| = \sqrt{EG - F^2}$, so the local surface area element is $dA = |\mathbf{X}_\alpha \times \mathbf{X}_\beta| d\alpha d\beta$.

3. Numerical method

In this section, we present the dimensionless governing equations of vesicle dynamics and their numerical discretizations. The discrete interface of vesicle is represented by the spherical harmonic expansion, so the spectral differentiations can be performed to achieve high accuracy of derivatives.

3.1. Dimensionless governing equations

For a vesicle interface enclosing the volume V , we define its effective radius $r = \left(\frac{3V}{4\pi}\right)^{1/3}$ as the characteristic length scale. The characteristic time scale for the vesicle under shear flow is defined by $t_c = 1/\dot{\gamma}$, where $\dot{\gamma}$ is the shear rate of flow. Then all the physical variables are scaled by the associated characteristic parameters as

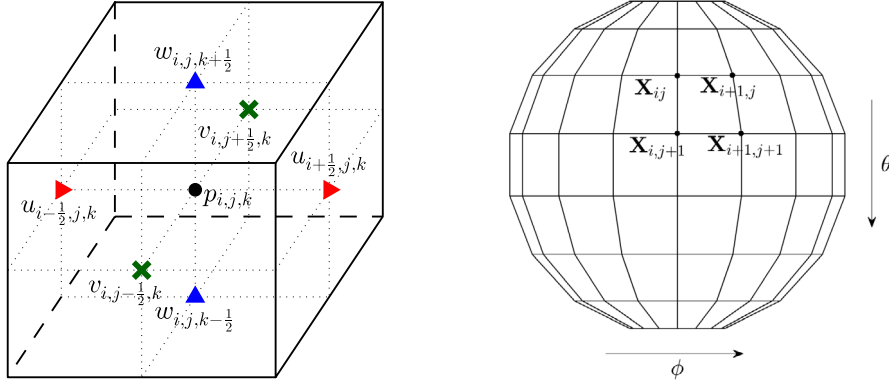


Fig. 1. Grid allocations for fluid variables u, v, w, p in Eulerian mesh (left) and for interfacial Lagrangian markers \mathbf{X} in spherical coordinates excluding poles (right). Here ϕ and θ denote the longitude and the colatitude, respectively.

$$\mathbf{x}^* = \frac{\mathbf{x}}{r}, \quad t^* = \frac{t}{t_c}, \quad \mathbf{u}^* = \frac{\mathbf{u}}{r/t_c}, \quad p^* = \frac{t_c}{\mu_o} p, \quad \sigma^* = \frac{t_c}{\mu_o} \sigma.$$

After performing a few calculations, the dimensionless governing equations of (1)-(8) can be written as (dropping the asterisk for convenience)

$$Re \left(\frac{\partial \mathbf{u}}{\partial t} + (\mathbf{u} \cdot \nabla) \mathbf{u} \right) = -\nabla p + \nabla \cdot [(1 + I(\lambda - 1)) (\nabla \mathbf{u} + \nabla \mathbf{u}^T)] + \mathbf{f} \quad \text{in } \Omega, \tag{15}$$

$$\nabla \cdot \mathbf{u} = 0 \quad \text{in } \Omega, \tag{16}$$

$$\mathbf{f}(\mathbf{x}, t) = \int_{\Gamma} (\mathbf{F}_\sigma + \mathbf{F}_b + \mathbf{F}_v) \delta(\mathbf{x} - \mathbf{X}(\alpha, \beta, t)) dA \quad \text{in } \Omega, \tag{17}$$

$$\frac{\partial \mathbf{X}}{\partial t}(\alpha, \beta, t) := \mathbf{U}(\alpha, \beta, t) = \int_{\Omega} \mathbf{u}(\mathbf{x}, t) \delta(\mathbf{x} - \mathbf{X}(\alpha, \beta, t)) d\mathbf{x} \quad \text{on } \Gamma, \tag{18}$$

$$\sigma(\alpha, \beta, t) = \sigma_0 \left(\frac{|\mathbf{X}_\alpha^0 \times \mathbf{X}_\beta^0|}{|\mathbf{X}_\alpha \times \mathbf{X}_\beta|} \right) \ln \left(\frac{|\mathbf{X}_\alpha \times \mathbf{X}_\beta|}{|\mathbf{X}_\alpha^0 \times \mathbf{X}_\beta^0|} \right) \quad \text{on } \Gamma, \tag{19}$$

$$\mathbf{F}_\sigma(\alpha, \beta, t) = \nabla_\Gamma \cdot (\sigma \mathbb{P}) = \nabla_\Gamma \sigma - 2\sigma H \mathbf{n} \quad \text{on } \Gamma, \tag{20}$$

$$\mathbf{F}_b(\alpha, \beta, t) = \frac{1}{2Ca} \left[\Delta_\Gamma H + 2H(H^2 - K) \right] \mathbf{n} \quad \text{on } \Gamma, \tag{21}$$

$$\mathbf{F}_v(\alpha, \beta, t) = -c_v \left(\frac{V(t) - V(0)}{V(0)} \right) \mathbf{n} \quad \text{on } \Gamma, \tag{22}$$

where

$$Re = \frac{\rho r^2}{\mu_o t_c}, \quad Ca = \frac{\mu_o r^3}{c_b t_c}, \quad \lambda = \frac{\mu_i}{\mu_o}.$$

Here, Re is the fluid Reynolds number, and Ca is the bending capillary number measuring the ratio of viscous force and bending force. The viscosity contrast between the interior and exterior fluids of vesicle is denoted by λ . We note that there is no dimensionless parameter in the elastic tension force \mathbf{F}_σ and the volume conservation force \mathbf{F}_v , since it can be absorbed into the respective stiffness parameters σ_0 and c_v which will be chosen later in practice.

Throughout this paper, we use spherical harmonics to represent a function defined on the interface. For convenience, we use spherical coordinates (ϕ, θ) to denote (α, β) in the following. So the vesicle interface $\Gamma(t)$ is a two-dimensional spherical surface represented by $\Gamma(t) = \{\mathbf{X}(\phi, \theta, t) = (X(\phi, \theta, t), Y(\phi, \theta, t), Z(\phi, \theta, t)) | 0 \leq \phi < 2\pi, 0 \leq \theta \leq \pi\}$, where ϕ is the longitude coordinate and θ is the colatitude, see the right of Fig. 1.

3.2. Spectral differentiation via spherical harmonic transform

As mentioned above, the vesicle surface is represented by spherical coordinates. In discrete setting, the longitudinal grid points are equi-spaced by $\phi_i = (i - 1)\Delta\phi$ with $\Delta\phi = 2\pi/N_\phi$ for $i = 1, \dots, N_\phi$. The colatitudinal grid points denoted by θ_j are the Gauss-Legendre quadrature nodes [37] with $\Delta\theta_j = \omega_j/\sin\theta_j$ and ω_j are the corresponding Gaussian quadrature weights for $j = 1, \dots, N_\theta$. As seen in the right of Fig. 1, the poles are not included.

One can approximate a real scalar function $f \in C^\infty(\mathbb{S}^2)$ by using the truncated spherical harmonic expansion as

$$f(\phi_i, \theta_j) \approx \sum_{n=0}^{p-1} \sum'_{m=0}^n P_n^m(\cos \theta_j) [a_{mn} \cos(m\phi_i) - b_{mn} \sin(m\phi_i)], \tag{23}$$

where p is an integer (we choose $p = N_\theta$ for simplicity), a_{mn} and b_{mn} are the real coefficients, and P_n^m denotes the associated Legendre function of degree n and order m [35,36]. Once the total number of frequency modes $p(p+1)/2$ is sufficient (depending on the smoothness of f), the above finite term approximation is known to be spectrally convergent. The primed sum in Eq. (23) denotes that the first term corresponding to $m = 0$ is multiplied by $1/2$. The constant $k_{mn} = \frac{(2n+1)(n-m)!}{2\pi(n+m)!}$ is used to normalize the above expansion, so the real coefficients in Eq. (23) are obtained by

$$a_{mn} = k_{mn} \sum_{i=1}^{N_\phi} \sum_{j=1}^{N_\theta} f(\phi_i, \theta_j) P_n^m(\cos \theta_j) \cos(m\phi_i) \sin \theta_j \Delta \theta_j \Delta \phi, \tag{24}$$

$$b_{mn} = k_{mn} \sum_{i=1}^{N_\phi} \sum_{j=1}^{N_\theta} f(\phi_i, \theta_j) P_n^m(\cos \theta_j) \sin(m\phi_i) \sin \theta_j \Delta \theta_j \Delta \phi. \tag{25}$$

Eqs. (24) and (25) constitute the forward scalar Spherical Harmonic Transform (SHT), while Eq. (23) is the corresponding backward scalar SHT. Note that, the SHT consists of the fast Fourier transform in the longitudinal (ϕ) direction and the Legendre transform in the colatitudinal (θ) direction. A detailed implementation for above transforms can be found in SPHEREPACK 3.2 [30].

A vector function or its derivative will likely be discontinuous at poles in the colatitude direction and it produces unbounded terms in PDEs posed in spherical coordinates [35]. More importantly, the discontinuity would lead to an unsatisfactory numerical accuracy due to slow convergence of the series in Eq. (23) [34]. This indicates that the scalar transform solely does not provide a suitable basis for discontinuous function. In computing derivatives of vector function, it is known that vector SHT helps to improve the numerical accuracy near two poles in spherical coordinates. Thus, for spectral differentiations of vector (and scalar) functions, we use the vector SHT presented in [35,36]. However, only the subroutines computing the first derivatives are provided in SPHEREPACK, so we need to develop the subroutines computing the second derivatives to obtain the bending force in Eq. (21).

The vector SHT introduces two basis functions

$$V_n^m(\theta) := \frac{1}{\sqrt{n(n+1)}} \frac{d}{d\theta} P_n^m(\cos \theta) \quad \text{and} \quad W_n^m(\theta) := \frac{1}{\sqrt{n(n+1)}} \frac{m}{\sin \theta} P_n^m(\cos \theta).$$

From this, one can compute the first derivatives of a real scalar component f of a vector function with respect to the longitude ϕ and the colatitude θ via the backward vector SHT as

$$\begin{aligned} \frac{\partial}{\partial \phi} f(\phi, \theta) &\approx \sum_{n=0}^{N_\theta-1} \sum'_{m=0}^n P_n^m(\cos \theta) [-mb_{mn} \cos(m\phi) - ma_{mn} \sin(m\phi)] \\ &= \sin \theta \sum_{n=0}^{N_\theta-1} \sum'_{m=0}^n \sqrt{n(n+1)} W_n^m(\theta) [-b_{mn} \cos(m\phi) - a_{mn} \sin(m\phi)], \end{aligned} \tag{26}$$

$$\frac{\partial}{\partial \theta} f(\phi, \theta) \approx \sum_{n=0}^{N_\theta-1} \sum'_{m=0}^n \sqrt{n(n+1)} V_n^m(\theta) [a_{mn} \cos(m\phi) - b_{mn} \sin(m\phi)]. \tag{27}$$

We shall implement the second-order numerical differentiations of f as

$$\frac{\partial^2}{\partial \phi^2} f(\phi, \theta) \approx \sum_{n=0}^{N_\theta-1} \sum'_{m=0}^n P_n^m(\cos \theta) [-m^2 a_{mn} \cos(m\phi) + m^2 b_{mn} \sin(m\phi)], \tag{28}$$

$$\frac{\partial^2}{\partial \phi \partial \theta} f(\phi, \theta) \approx \sum_{n=0}^{N_\theta-1} \sum'_{m=0}^n \sqrt{n(n+1)} V_n^m(\theta) [-mb_{mn} \cos(m\phi) - ma_{mn} \sin(m\phi)], \tag{29}$$

$$\frac{\partial^2}{\partial \theta^2} f(\phi, \theta) \approx \sum_{n=0}^{N_\theta-1} \sum'_{m=0}^n \frac{d^2}{d\theta^2} P_n^m(\cos \theta) [a_{mn} \cos(m\phi) - b_{mn} \sin(m\phi)], \tag{30}$$

where

$$\begin{aligned} \frac{d^2}{d\theta^2} P_n^m(\cos\theta) &= -\cot\theta \frac{d}{d\theta} P_n^m(\cos\theta) + \left(\frac{m^2}{\sin^2\theta} - n(n+1) \right) P_n^m(\cos\theta) \\ &= -\cot\theta \sqrt{n(n+1)} V_n^m(\theta) + \frac{m^2}{\sin^2\theta} P_n^m(\cos\theta) - n(n+1) P_n^m(\cos\theta). \end{aligned}$$

The equality of $\frac{d^2}{d\theta^2} P_n^m(\cos\theta)$ holds due to the property of the associated Legendre function or polynomial. To perform numerical differentiation, we first obtain the real coefficients (24) and (25) by applying forward scalar SHT, then modify the coefficients according to Eqs. (26)-(30). Using the modified coefficients in particular for second derivatives, the backward scalar SHT can be applied to obtain $\frac{\partial^2 f}{\partial \phi^2}$ in Eq. (28), while the backward vector SHT is applied to obtain $\frac{\partial^2 f}{\partial \phi \partial \theta}$ in Eq. (29). To obtain $\frac{\partial^2 f}{\partial \theta^2}$ in Eq. (30), we especially need to apply the backward vector SHT once and the backward scalar SHT twice in a term-by-term manner. Notice that the functions of θ such as $\cot\theta$ and $1/\sin^2\theta$ shall be multiplied after transforms. Throughout this paper, we will use the SHT to spectrally differentiate the vesicle surface position vector $\mathbf{X}(\phi, \theta)$ as mentioned above to get all the fundamental forms needed to compute the mean curvature H and Gaussian curvature K (Eq. (10)), the surface gradient of elastic tension $\nabla_\Gamma \sigma(\phi, \theta)$ (Eq. (11)), the surface divergence of interfacial velocity $\nabla_\Gamma \cdot \mathbf{U}(\phi, \theta)$ (Eq. (12)), and the elastic tension force $\nabla_\Gamma \cdot [\sigma(\phi, \theta) \mathbb{P}(\phi, \theta)]$ (Eq. (20)).

However, the computation of surface Laplacian of mean curvature $\Delta_\Gamma H$ used in bending force term involves second-order partial derivatives for the mean curvature; thus, the fourth-order partial derivatives for the position vector. As one can see, the spectral differentiation higher than second-order with respect to the colatitude direction is more complicated. To compute $\Delta_\Gamma H$ more accurately by using only first- and second-order differentiations, we employ the following *upsampling algorithm* used in [40] to enhance the numerical accuracy.

For the given discrete position vector \mathbf{X} with the N_ϕ -by- N_θ size, we compute $\Delta_\Gamma H$ defined at \mathbf{X} in the step-by-step numerical procedure as follows.

- Step 1. Apply component-wisely the forward Spherical Harmonic Transform (SHT) onto \mathbf{X} , as described in Eqs. (24) and (25), to obtain the coefficients with the N_θ -by- N_θ size. (Note that we use an N_θ -by- N_θ rectangular matrix in practice for convenience, while the definition of spherical harmonic expansion in Eq. (23) has a triangular domain of frequency modes.) According to Eqs. (26)-(30), modify the coefficients to compute the first and second partial derivatives. Pad zeros to the modified coefficients by extending high frequency modes so that the new coefficients have the $2N_\theta$ -by- $2N_\theta$ size.
- Step 2. Apply the backward SHT onto the extended coefficients to obtain the upsampled partial derivatives with the $2N_\phi$ -by- $2N_\theta$ size. By using the upsampled derivatives, compute the upsampled H with the $2N_\phi$ -by- $2N_\theta$ size by Eq. (10).
- Step 3. Apply the first-order spectral differentiation to the upsampled H , then compute the upsampled $\Delta_\Gamma H$ referring to Eq. (14). To downsample, apply the forward SHT to the upsampled $\Delta_\Gamma H$, then apply the backward SHT onto the shrinking coefficients with the N_θ -by- N_θ size.

3.3. Numerical scheme

In this subsection, we present the numerical scheme and the related implementation details for solving the dimensionless governing equations (15)-(22). Throughout this paper, the Dirichlet boundary condition is imposed for the fluid velocity in all directions. To solve the Navier-Stokes equations (15)-(16) in a computational domain $\Omega \subset \mathbb{R}^3$, we layout a uniform Cartesian grid with mesh width $h = \Delta x = \Delta y = \Delta z$, and allocate the fluid velocity $\mathbf{u} = (u, v, w)$ and the pressure p in a staggered marker-and-cell (MAC) grid manner [14], see the left of Fig. 1.

To discretize the vesicle interface \mathbf{X} , we apply the spherical harmonic expansion (23) in a component-wise manner as

$$\begin{aligned} \mathbf{X}(\phi_i, \theta_j) &= (X(\phi_i, \theta_j), Y(\phi_i, \theta_j), Z(\phi_i, \theta_j)) \\ &\approx \sum_{n=0}^{N_\theta-1} \sum_{m=0}^n P_n^m(\cos\theta_j) \left[\left(a_{mn}^X, a_{mn}^Y, a_{mn}^Z \right) \cos(m\phi_i) - \left(b_{mn}^X, b_{mn}^Y, b_{mn}^Z \right) \sin(m\phi_i) \right], \end{aligned}$$

where each component of the coefficient vectors, $(a_{mn}^X, a_{mn}^Y, a_{mn}^Z)$ and $(b_{mn}^X, b_{mn}^Y, b_{mn}^Z)$, corresponds to that of coordinate (X, Y, Z) , respectively. We differentiate this representation from the radial approximation of vesicle interface used in [41], wherein the position vector contains a single scalar variable as a function of (ϕ, θ) , namely the radial deviation from a sphere. For $i = 1, \dots, N_\phi$ and $j = 1, \dots, N_\theta$, the discrete interface is represented by a set of Lagrangian markers $\mathbf{X}_{ij} = \mathbf{X}(\phi_i, \theta_j)$ and other variables are defined in a similar manner. The associated geometric quantities and their derivatives are all computed at \mathbf{X}_{ij} . For this, the spectral partial derivatives with respect to ϕ and θ up to second-order can be computed efficiently and accurately as described in Subsection 3.2. One can also refer to [8,18] for the applications of spherical harmonic representation to stationary vesicle and molecular surfaces.

We now present how to march the Lagrangian markers $\mathbf{X}^k = \mathbf{X}(k\Delta t)$ from time level k to $\mathbf{X}^{k+1} = \mathbf{X}((k+1)\Delta t)$ at time level $k+1$, where Δt is the time step size. In the following, the fluid velocity \mathbf{u}^k , the pressure p^k , and the Lagrangian

markers \mathbf{X}^k are all given in advance, and from these variables we seek to update \mathbf{u}^{k+1} , p^{k+1} , and \mathbf{X}^{k+1} . The step-by-step numerical procedure can be done as follows.

Step 1. At the Lagrangian markers \mathbf{X}_{ij}^k , we compute the first and second derivatives of the surface position vector \mathbf{X} by applying the spectral differentiations described in the Subsection 3.2. The discrete outward normal vector is obtained by

$$\mathbf{n}_{ij}^k = \frac{\mathbf{X}_{\theta,ij}^k \times \mathbf{X}_{\phi,ij}^k}{|\mathbf{X}_{\theta,ij}^k \times \mathbf{X}_{\phi,ij}^k|},$$

where $\mathbf{X}_{\theta,ij}^k$ and $\mathbf{X}_{\phi,ij}^k$ denote the first derivatives of \mathbf{X}_{ij}^k with respect to θ and ϕ , respectively. The discrete projection operator is then obtained by

$$\mathbb{P}_{ij}^k = \mathbb{I} - \mathbf{n}_{ij}^k (\mathbf{n}_{ij}^k)^T.$$

Referring to Eqs. (10) and (14), the discrete geometric quantities can be further obtained. For the Gaussian quadrature weight ω , the discrete local surface area is obtained from

$$dA_{ij}^k = |\mathbf{X}_{\theta,ij}^k \times \mathbf{X}_{\phi,ij}^k| \Delta\phi \Delta\theta_j = |\mathbf{X}_{\theta,ij}^k \times \mathbf{X}_{\phi,ij}^k| \Delta\phi \omega_j / \sin\theta_j.$$

So for a given constant σ_0 , the numerical elastic tension in Eq. (19) can be computed by

$$\sigma_{ij}^k = \sigma_0 \left(\frac{dA_{ij}^{0,k}}{dA_{ij}^k} \right) \ln \left(\frac{dA_{ij}^k}{dA_{ij}^{0,k}} \right). \tag{31}$$

We leave the computation of $dA_{ij}^{0,k}$ later in Eq. (32) due to the modification of tangential velocity.

Once we have σ_{ij}^k , the discrete elastic tension force \mathbf{F}_σ can be computed in two different forms as in Eq. (20). The divergence form is computed by applying Eq. (12) component-wisely to $\nabla_{\Gamma_h} \cdot (\sigma_{ij}^k \mathbb{P}_{ij}^k)$. More specifically, the m -th component of $\mathbf{F}_\sigma(\mathbf{X}_{ij}^k)$ for $m = 1, 2, 3$ is obtained by computing

$$\nabla_{\Gamma_h} \cdot (\sigma_{ij}^k \mathbb{P}_{m1,ij}^k, \sigma_{ij}^k \mathbb{P}_{m2,ij}^k, \sigma_{ij}^k \mathbb{P}_{m3,ij}^k),$$

where $\mathbb{P}_{mn,ij}^k$ is the (m, n) -th element of the 3-by-3 matrix \mathbb{P}_{ij}^k . The non-divergence form written in $\nabla_{\Gamma_h} \sigma_{ij}^k - 2\sigma_{ij}^k H_{ij}^k \mathbf{n}_{ij}^k$ is obtained by Eq. (11) for the tangential component and by the discrete mean curvature normal vector for the normal component. A numerical comparison of those two formulations for computing elastic tension force will be given in Subsection 4.2, where we demonstrate that using the divergence form is numerically more stable.

Meanwhile, in computing the bending force \mathbf{F}_b , we employ the upsampling algorithm to enhance numerical accuracy of the discrete surface Laplacian of mean curvature. The detailed implementation is already given in the end of Subsection 3.2 and the related numerical result will be discussed later in Subsection 4.1. To compute the volume conservation force \mathbf{F}_v in Eq. (22), we use the formula for the enclosed volume

$$V^k = \frac{1}{3} \sum_{i=1}^{N_\phi} \sum_{j=1}^{N_\theta} \mathbf{X}_{ij}^k \cdot \mathbf{n}_{ij}^k dA_{ij}^k,$$

as an approximation of $V(t) = \frac{1}{3} \int_{\Gamma(t)} \mathbf{X} \cdot \mathbf{n} dA$.

Step 2. Distribute the interfacial forces acting on Lagrangian markers into the Eulerian grid $\mathbf{x} = (x, y, z)$ by means of the smoothed Dirac delta function δ_h as

$$\mathbf{f}^k(\mathbf{x}) = \sum_{i=1}^{N_\phi} \sum_{j=1}^{N_\theta} \left[\mathbf{F}_\sigma(\mathbf{X}_{ij}^k) + \mathbf{F}_b(\mathbf{X}_{ij}^k) + \mathbf{F}_v(\mathbf{X}_{ij}^k) \right] \delta_h(\mathbf{x} - \mathbf{X}_{ij}^k) dA_{ij}^k.$$

Here for the discrete delta function $\delta_h(\mathbf{x}) = \frac{1}{h^3} \varphi(\frac{x}{h}) \varphi(\frac{y}{h}) \varphi(\frac{z}{h})$, we employ the 4-point supported function φ developed in [44] to suppress spurious force oscillations in IB method.

Step 3. Solve the Navier-Stokes equations by the second-order incremental pressure-correction projection method presented in [12] as follows.

$$\begin{aligned}
 & Re \left[\frac{3\mathbf{u}^* - 4\mathbf{u}^k + \mathbf{u}^{k-1}}{2\Delta t} + 2(\mathbf{u}^k \cdot \nabla_h)\mathbf{u}^k - (\mathbf{u}^{k-1} \cdot \nabla_h)\mathbf{u}^{k-1} \right] \\
 &= -\nabla_h p^k + \lambda \Delta_h \mathbf{u}^* + \nabla_h \cdot \left[(\lambda - 1)(I^k - 1)(\nabla_h \mathbf{u}^k + \nabla_h^T \mathbf{u}^k) \right] + \mathbf{f}^k, \\
 \Delta_h p^* &= \frac{3Re}{2\Delta t} \nabla_h \cdot \mathbf{u}^*, \quad \frac{\partial p^*}{\partial \mathbf{n}} = 0 \text{ on } \partial\Omega, \quad \mathbf{u}^* = \mathbf{u}^{k+1} \text{ on } \partial\Omega, \\
 \mathbf{u}^{k+1} &= \mathbf{u}^* - \frac{2\Delta t}{3Re} \nabla_h p^*, \quad \nabla_h p^{k+1} = \nabla_h p^* + \nabla_h p^k - \frac{2\lambda \Delta t}{3Re} \Delta_h (\nabla_h p^*),
 \end{aligned}$$

where the discrete operators ∇_h and $\nabla_h \cdot$ approximate the gradient and divergence operators, respectively, using the second-order finite difference in staggered grid. For the nonlinear terms, the skew-symmetric form is employed as $(\mathbf{u} \cdot \nabla_h) \mathbf{u} = \frac{1}{2} (\mathbf{u} \cdot \nabla_h) \mathbf{u} + \frac{1}{2} \nabla_h (\mathbf{u} \mathbf{u})$. The viscous term represented above by \mathbf{u}^* and \mathbf{u}^k is equivalent to

$$\lambda \Delta_h \mathbf{u}^* - \lambda \Delta_h \mathbf{u}^k + \nabla_h \cdot \left[(1 + I^k(\lambda - 1)) (\nabla_h \mathbf{u}^k + \nabla_h^T \mathbf{u}^k) \right],$$

which implies that the more viscous inner fluid of vesicle is treated implicitly while the less viscous outer fluid is treated explicitly. In order to obtain the discrete indicator (or regularized Heaviside) function $I^k(\mathbf{x})$ at the k -th time step, we solve the discrete Poisson equation with either zero Dirichlet or Neumann boundary condition as developed in [38] by

$$\Delta_h I^k(\mathbf{x}) = -\nabla_h \cdot \sum_{i=1}^{N_\phi} \sum_{j=1}^{N_\theta} \mathbf{n}_{ij}^k \delta_h(\mathbf{x} - \mathbf{X}_{ij}^k) dA_{ij}^k,$$

whose continuous counterpart is

$$\Delta I(\mathbf{x}, t) = -\nabla \cdot \int_{\Gamma} \mathbf{n} \delta(\mathbf{x} - \mathbf{X}(\phi, \theta, t)) dA.$$

In solving Poisson and Helmholtz equations stated in this step, a fast solver using fast sine (cosine) transform can be exploited for the Dirichlet (Neumann) boundary condition.

Step 4. In this step, we interpolate the interfacial velocity of fluidic vesicle as

$$\mathbf{U}_{ij}^{k+1} = \sum_{\mathbf{x}} \mathbf{u}^{k+1}(\mathbf{x}) \delta_h(\mathbf{x} - \mathbf{X}_{ij}^k) h^3.$$

In traditional IB method, we then advance the Lagrangian markers to new positions by $\mathbf{X}_{ij}^{k+1} = \mathbf{X}_{ij}^k + \Delta t \mathbf{U}_{ij}^{k+1}$ as a discretization of $\frac{\partial \mathbf{X}}{\partial t} = \mathbf{U}$ in Eq. (18), i.e., no-slip condition. However, the tank-treading and tumbling motions of vesicle under shear flow will lead to a distortion of the interfacial mesh, so we take a different approach to advance the markers. Our goal is to attenuate such distortion, thus to improve the numerical stability over the traditional approach. To this end, we apply the forward SHT to \mathbf{U}_{ij}^{k+1} , then adopt the 2/3-rule filter for dealiasing the normal velocity component. On the other hand, for the tangential velocity component, we keep only 15 lower frequencies to smooth out the tangential velocity. (Notice that, changing the tangential velocity does not affect the shape of vesicle interface.) Denoting this filtered velocity by $\tilde{\mathbf{U}}^{k+1}$, the interfacial mesh is now updated more smoothly by (as a discretization of $\frac{\partial \mathbf{X}}{\partial t} = \tilde{\mathbf{U}}$)

$$\mathbf{X}_{ij}^{k+1} = \mathbf{X}_{ij}^k + \Delta t \tilde{\mathbf{U}}_{ij}^{k+1}.$$

Step 5. Update the local surface element $dA_{ij}^{0,k+1}$ used in Eq. (31). Since the tangential velocity is modified via smoothing, the initial local surface area element used in Eq. (31) must be modified accordingly. In other words, when the Lagrangian markers move by modified tangential velocity, the (initially obtained) target local surface area $dA^{0,k+1}$ at the $(k+1)$ -th time step should be newly updated according to

$$\frac{dA_{ij}^{0,k+1}}{\sum_{i=1}^{N_\phi} \sum_{j=1}^{N_\theta} dA_{ij}^0} = \frac{\tilde{dA}_{ij}^{0,k+1}}{\sum_{i=1}^{N_\phi} \sum_{j=1}^{N_\theta} \tilde{dA}_{ij}^{0,k+1}}, \tag{32}$$

where

$$\ln \tilde{dA}_{ij}^{0,k+1} = \ln dA_{ij}^{0,k} + \Delta t \nabla_{\Gamma_h} \cdot \left[\mathbb{P}_{ij}^k (\tilde{\mathbf{U}}_{ij}^{k+1} - \mathbf{U}_{ij}^{k+1}) \right]. \tag{33}$$

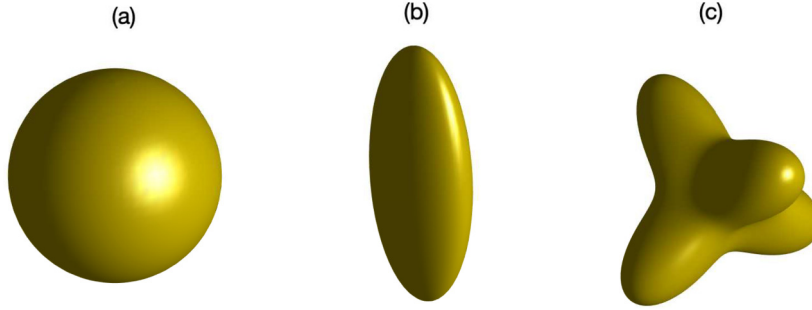


Fig. 2. Three geometries. (a) the unit sphere; (b) the ellipsoid with aspect ratio 1 : 2 : 4; (c) the complex surface using the spherical harmonic Y_3^2 .

Eq. (32) is simply the normalization for each target local surface area so that the total surface area is conserved as the original one. However, Eq. (33) is obtained by an approximation of the following evolution equation of local surface area

$$\begin{aligned} \frac{\partial(\ln|\mathbf{X}_\theta \times \mathbf{X}_\phi|)}{\partial t} &= \frac{1}{|\mathbf{X}_\theta \times \mathbf{X}_\phi|} \frac{\partial|\mathbf{X}_\theta \times \mathbf{X}_\phi|}{\partial t} = \nabla_\Gamma \cdot \frac{\partial \mathbf{X}}{\partial t} \quad (\text{from [31, Eq. (12)]}) \\ &= \nabla_\Gamma \cdot \tilde{\mathbf{U}} = \nabla_\Gamma \cdot [\mathbf{U} + \mathbb{P}(\tilde{\mathbf{U}} - \mathbf{U})] \quad (\text{by } \frac{\partial \mathbf{X}}{\partial t} := \tilde{\mathbf{U}}) \\ &\approx \nabla_\Gamma \cdot [\mathbb{P}(\tilde{\mathbf{U}} - \mathbf{U})] \quad (\nabla_\Gamma \cdot \mathbf{U} \approx 0 \text{ for nearly incompressible interface}). \end{aligned}$$

4. Numerical results

In this section, we begin by checking the numerical accuracy of discrete geometric quantities needed in computing the bending force. Then a numerical stability issue arising from the necessity of using divergence form for elastic tension force is investigated together with convergence analysis of primitive variables and conservative quantities. Afterwards, a series of numerical experiments are performed for a vesicle under shear flow, whereby the effects of dimensionless parameters such as the reduced volume, bending capillary number, viscosity contrast, and the Reynolds number are extensively studied. A study on vesicle deformation under Poiseuille flow is also carried out.

4.1. Accuracy check on some geometrical quantities

We first examine the numerical accuracy of geometric quantities associated with the bending force in Eq. (21) such as the mean curvature H , Gaussian curvature K , and the surface Laplacian of mean curvature $\Delta_\Gamma H$. Throughout this paper, we fix $N_\phi = 2N_\theta$, so the computed solution with $2N_\theta$ -by- N_θ size is used for simplicity, although our method allows almost arbitrary size. For spherical coordinates

$$(X(\phi, \theta), Y(\phi, \theta), Z(\phi, \theta)) = (a(\phi, \theta) \sin \theta \cos \phi, b(\phi, \theta) \sin \theta \sin \phi, c(\phi, \theta) \cos \theta),$$

we test three different geometries as illustrated in Fig. 2

- Sphere: $a = b = c = 1$
- Ellipsoid: $a = 1, b = 2, c = 4$
- Complex surface using Y_3^2 : $a = b = c = 1 + e^{-3\Re(Y_3^2)}$,

where the term $\Re(Y_3^2)$ denotes the real part of the spherical harmonic function $Y_3^2(\phi, \theta) = \frac{1}{4} \sqrt{\frac{105}{2\pi}} e^{i2\phi} \sin^2 \theta \cos \theta$.

In Table 1, the maximum norm errors of H , K , and $\Delta_\Gamma H$ are provided for the three geometries. We set $N_\phi = 2N_\theta$ as aforementioned, so the total number of surface points is $N_\phi N_\theta = 2N_\theta^2$. As shown in the table, the errors of H and K are spectrally accurate as expected. (Note that the error increases somewhat as N_θ increases due to the inheritance of spectral approximation where the summation of more terms accumulates the machine error.)

However, the errors of $\Delta_\Gamma H$ without upsampling (denoted by $\|\Delta_\Gamma H\|_\infty$) and with upsampling (denoted by $\|\widetilde{\Delta_\Gamma H}\|_\infty$) do show significant difference as the latter one shows better accuracy. For the unit sphere, we observe that both errors are similar in magnitude regardless of the use of upsampling. This is not surprising since a sphere has constant curvature so $\Delta_\Gamma H$ vanishes, meaning that only a few numbers of frequency modes in spherical harmonics are needed. For other two geometries (an ellipsoid and complex surface), the errors of $\Delta_\Gamma H$ obtained without the upsampling method are nearly constant for any N_θ , while those with the upsampling are relatively reduced by a factor of 100 for $N_\theta \geq 64$. In the case of the ellipsoid with aspect ratio 1 : 2 : 4, the maximum values of three quantities estimated numerically are $\max(H) =$

Table 1
 For the three geometries plotted in Fig. 2, the maximum numerical errors of the mean curvature H , Gaussian curvature K , and the surface Laplacian of mean curvature (without upsampling $\Delta_\Gamma H$, with upsampling $\|\widetilde{\Delta_\Gamma H}\|_\infty$).

N_θ	$\ H\ _\infty$	$\ K\ _\infty$	$\ \Delta_\Gamma H\ _\infty$	$\ \widetilde{\Delta_\Gamma H}\ _\infty$
<i>(The unit sphere)</i>				
16	4.02×10^{-13}	8.04×10^{-13}	1.26×10^{-10}	1.15×10^{-10}
32	4.37×10^{-12}	8.74×10^{-12}	1.59×10^{-8}	6.15×10^{-9}
64	3.17×10^{-11}	6.34×10^{-11}	5.06×10^{-7}	1.46×10^{-7}
128	3.98×10^{-10}	7.97×10^{-10}	4.28×10^{-5}	8.35×10^{-6}
<i>(The ellipsoid with aspect ratio 1 : 2 : 4)</i>				
16	3.08×10^{-13}	4.58×10^{-13}	5.71×10^1	3.59×10^1
32	7.53×10^{-12}	1.44×10^{-11}	3.27×10^1	4.16×10^0
64	2.69×10^{-11}	7.84×10^{-11}	2.48×10^1	2.30×10^{-1}
128	4.83×10^{-10}	1.01×10^{-9}	2.33×10^1	2.24×10^{-1}
<i>(The complex surface using the spherical harmonic Y_3^2)</i>				
16	8.14×10^{-3}	6.74×10^{-3}	5.82×10^0	4.49×10^0
32	4.53×10^{-9}	7.24×10^{-9}	4.20×10^0	2.08×10^0
64	2.91×10^{-11}	3.74×10^{-11}	2.69×10^0	6.44×10^{-2}
128	3.41×10^{-10}	3.70×10^{-10}	2.64×10^0	2.69×10^{-2}

2.5, $\max(K) = 4$, and $\max(\Delta_\Gamma H) = 100$. Similar values are also obtained in the case of the complex surface, but with more complex variation of geometric quantities. Taking these maximum values into account, we can conclude that the contribution of $\Delta_\Gamma H$ is considerably larger than $2H(H^2 - K)$ term in bending resistance, thus even a slight improvement of accuracy of $\Delta_\Gamma H$ will have significant influence on vesicle motion. Therefore, in computing bending force, we shall apply the upsampling method to compute the surface Laplacian of mean curvature.

Before closing this subsection, we remark a few limitations of using spherical harmonic expansion to represent the vesicle surface. As known, each surface representation method has pros and cons in terms of accuracy and versatility. There is certainly a trade-off between the accuracy and flexibility that we should consider in the development of numerical methods. As verified above for fixed geometries, the use of spectral method is able to achieve high accuracy for computing geometric quantities of spherical surfaces. However, the method can only approximate moderately deformed surfaces as seen in Fig. 2(c), and the applications are limited to quasi-spherical vesicles as shown in the subsequent subsections. As mentioned in the introduction of [9], however, highly deformed surface such as tethered vesicle can take very long and thin shapes. In that case, sufficiently large number of spherical harmonics is required to properly approximate within desired accuracy so the associated computational time would increase accordingly. Meanwhile, the spherical coordinate representation of an evolving vesicle is difficult to apply adaptive mesh refinement for interfaces with high curvature region. Despite that, to maintain the interfacial mesh quality, a new mesh control technique via filtering of interfacial tangential velocity is proposed and has been confirmed useful in this paper. We also note that the spectral representation using spherical harmonic expansion is developed to approximate a function defined on a sphere, so such representation is only applicable to spherical surfaces with genus zero. Therefore, to approximate surfaces of arbitrary shapes or topologies, one may need to use a triangulation instead. However, from the accuracy point of view, the computation of geometric quantities, in particular $\Delta_\Gamma H$, would not converge on triangulation when the mesh is refined as reported in [11], while the computation via the present spectral method with upsampling can converge satisfactorily as shown in Table 1.

4.2. Numerical stability of elastic tension force computation

As mentioned earlier in Eq. (6), there are two equivalent forms of elastic tension force; namely, the divergence form $\nabla_\Gamma \cdot (\sigma \mathbb{P})$ and the non-divergence form $\nabla_\Gamma \sigma - 2\sigma H \mathbf{n}$. Here, we investigate the numerical stability about the usage of both forms for the problem of vesicle relaxation in quiescent flow. To see more clearly, we test two types of vesicles initially given by an oblate with aspect ratio 3 : 3 : 1 and a prolate with the aspect ratio 1 : 1 : 2.8. For an ellipsoidal vesicle with aspect ratio $a : b : c$, the lengths of semi-axes are normalized by $(abc)^{1/3}$ so that the enclosed volume is fixed by $V = 4\pi/3$. For a given initial vesicle shape, another dimensionless number measuring the volume ratio between the vesicle shape and the sphere with the same surface area is called the *reduced volume* and is defined by $v = \frac{3V}{4\pi (A/4\pi)^{3/2}}$, where A is the surface area of the vesicle. In this test, we set the computational domain by $[-3, 3]^3$, the grid mesh width by $h = 6/N$ with $N = 64$, and the time step size by $\Delta t = 1/(6N)$. The total number of Lagrangian markers is $2N_\theta^2$ with $N_\theta = N/2$, and the dimensionless parameters are set by $Re = 1$, $Ca = 2.5$, $\lambda = 1$, $\sigma_0 = 9.375N$, and $c_v = 0$. Throughout this paper, the same computational setup is used unless otherwise stated.

In Fig. 3(a-c, g-i), the temporal evolution of vesicle shapes by using divergence form of tension force in our scheme is quite stable. These shapes are smooth and nearly axisymmetric as desired. On the contrary, when the non-divergence form is used as shown in Fig. 3(d-f, j-l), the unphysical oscillatory shapes emerge along the longest axis at earlier time and they soon blow up (the computational times of Fig. 3(f, l) are only up to $t = 1.3$ and $t = 2.58$, respectively). We

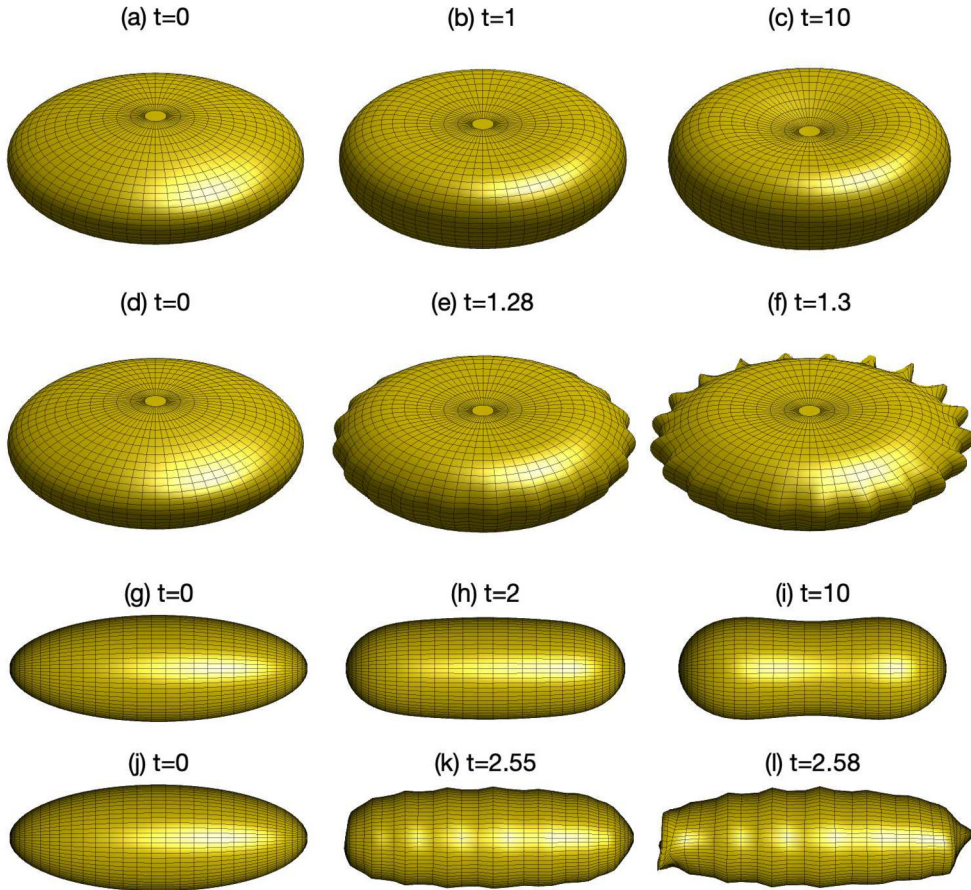


Fig. 3. For initially oblate and prolate vesicles, their temporal evolution by using the divergence form of tension force in (a-c) and (g-i); by the non-divergence form in (d-f) and (j-l).

attribute such instability to the imbalance of tension force in the tangential and normal directions. To see this, suppose all the geometric quantities are spectrally accurate and the elastic tension is represented by $\sigma(\theta, \phi) = \sigma_e(\theta, \phi) + \varepsilon(\theta, \phi)$, where σ_e is the exact solution and ε is the numerical error. So the two forms of discrete tension force take the divergence form $\nabla_{\Gamma_h} \cdot [(\sigma_e + \varepsilon)\mathbb{P}]$, and the non-divergence form $\nabla_{\Gamma_h}(\sigma_e + \varepsilon) - 2(\sigma_e + \varepsilon)H\mathbf{n}$. One can see that the divergence form has the error magnitude of $\nabla_{\Gamma_h} \cdot (\varepsilon\mathbb{P})$ in all x, y, z directions, while the non-divergence form has the error of $\nabla_{\Gamma_h} \varepsilon$ in the tangential direction and $2\varepsilon H\mathbf{n}$ in the normal direction. Because the difference between the error ε and its derivative is quite different in magnitude, it appears that such imbalance of elastic tension force in non-divergence form can eventually cause the simulation failed as we can see in the test. Consequently, regardless of geometry used in Fig. 3, the divergence form is able to keep the computation stable during vesicle relaxation in quiescent flow. Therefore, it will greatly help to stabilize the vesicle dynamics in various flows so we only employ the divergence form of the discrete elastic tension force in the rest of simulations.

4.3. Convergence study

Next, we study the numerical convergence behavior of primitive variables and conservative quantities for the present scheme. The computational setup is basically same to that used for the vesicle relaxation simulation presented in the previous subsection. The initial vesicle is an oblate with same aspect ratio as previously described. We run the simulations with different resolutions $N = 32, 64, 128, 256$ (the mesh width is $h = 6/N$), and calculate the order of accuracy of velocity component u via three successive results as

$$\text{Order} = \log_2 \left(\frac{\|u_{2h} - u_{4h}\|_2}{\|u_h - u_{2h}\|_2} \right).$$

Other variables can be obtained in a similar manner. Note that the resolution of vesicle interface shall be refined as that of fluid grid mesh is refined; that is, the number of total Lagrangian markers on the vesicle interface is $N^2/2$, as mentioned earlier in Subsection 4.2. The results are computed up to time $t = 0.5$.

Table 2

Convergence analysis of the relative errors of the fluid velocity (u, v, w), fluid pressure p , and the position vector \mathbf{X} at $t = 0.5$. Here \bar{h} denotes the finest resolution used in this study, so $\bar{h} = 6/256$.

h	$\frac{\ u_h - u_{2h}\ _2}{\ u_{\bar{h}}\ _2}$	Order	$\frac{\ v_h - v_{2h}\ _2}{\ v_{\bar{h}}\ _2}$	Order	$\frac{\ w_h - w_{2h}\ _2}{\ w_{\bar{h}}\ _2}$	Order
6/64	5.200×10^{-1}	-	5.233×10^{-1}	-	4.478×10^{-1}	-
6/128	1.007×10^{-1}	2.36	1.016×10^{-1}	2.36	9.260×10^{-2}	2.27
6/256	3.148×10^{-2}	1.67	3.235×10^{-2}	1.65	2.636×10^{-2}	1.81
h	$\frac{\ p_h - p_{2h}\ _2}{\ p_{\bar{h}}\ _2}$	Order	$\frac{\ \mathbf{X}_h - \mathbf{X}_{2h}\ _2}{\ \mathbf{X}_{\bar{h}}\ _2}$	Order		
6/64	3.598×10^{-1}	-	1.012×10^{-2}	-		
6/128	1.230×10^{-1}	1.54	2.140×10^{-3}	2.24		
6/256	7.203×10^{-2}	0.77	5.738×10^{-4}	1.89		

Table 3

The maximum (relative) errors of the surface divergence of interfacial velocity $\nabla_\Gamma \cdot \mathbf{U}$, the local surface area dA , the total surface area A , and the enclosed volume V at $t = 0.5$.

h	$\ \nabla_\Gamma \cdot \mathbf{U}\ _\infty$	$\left\ \frac{dA(t) - dA(0)}{dA(0)} \right\ _\infty$	$\left \frac{A(t) - A(0)}{A(0)} \right $	$\left \frac{V(t) - V(0)}{V(0)} \right $
6/32	8.710×10^{-3}	8.218×10^{-3}	2.112×10^{-3}	7.928×10^{-5}
6/64	2.013×10^{-3}	1.466×10^{-3}	9.486×10^{-4}	2.631×10^{-5}
6/128	3.364×10^{-4}	5.039×10^{-4}	4.493×10^{-4}	6.671×10^{-6}
6/256	1.221×10^{-4}	2.494×10^{-4}	2.233×10^{-4}	7.250×10^{-6}

Table 2 shows the L_2 -errors of primitive variables such as the fluid velocity (u, v, w), the pressure p , and the position vector \mathbf{X} at time $t = 0.5$. Since the exact solution is unknown in this test, we evaluate the error of two numerical solutions obtained in successive resolutions and then divide by the numerical solution obtained in the finest resolution ($\bar{h} = 6/256$). As shown in the table, the overall order of accuracy of all variables confirms that our numerical solutions converge well. Although the numerical orders of fluid velocity and pressure obtained here are a little higher than predicted in theory [5], but we believe that the actual accuracy would be lower as we refine the computational resolution. The accuracy of the position vector \mathbf{X} is also consistent with that obtained in [26].

Table 3 shows the maximum (relative) errors associated with conservative quantities of vesicle, such as the local interfacial incompressibility $\nabla_\Gamma \cdot \mathbf{U} = 0$, local surface area dA , total surface area A , and the enclosed volume V . We clearly see that all the quantities are conserved well and tend to converge further as the resolution is refined.

4.4. Tank-treading motion under shear flow

In this subsection, we impose the shear flow $\mathbf{u} = (z, 0, 0)$ on the fluid domain boundary to see the vesicle tank-treading motion. Here, we assume that the viscosities of inner and outer fluids of vesicle match under Stokes regime, so we fix $\lambda = 1$ and $Re = 10^{-3}$. The capillary number associated with bending resistance is also set by $Ca = 2.5$. Throughout this subsection to Subsection 4.6, we use a larger domain $[-6, 6]^3$ to avoid the effect of computational domain size on vesicle dynamics. The grid number in each coordinate direction is chosen as $N = 128$, and the time step size is chosen as $\Delta t = 1/(3N)$. The discrete interface of initially prolate vesicle is represented by the $2N_\theta^2$ number of Lagrangian markers with $N_\theta = N/2$. The dimensionless parameter for volume conservation is fixed by $c_v = 10^5$.

In Fig. 4, the temporal evolution of tank-treading vesicles with reduced volume (defined earlier in Subsection 4.2) $\nu = 0.975, 0.9, 0.8$ is depicted. As ν decreases, the interfacial shape gets longer and thinner, and the interfacial mesh distorts more severely. Although not shown here, the simulation breaks down at early time if the filtering method for interfacial tangential velocity presented in Step 4 of Subsection 3.3 is not applied. So, under the spherical harmonic representation of vesicle interface, an adequate mesh control plays an important role to enhance the numerical stability.

To see whether the present IB method simulates correctly the essential physics of tank-treading vesicle in Stokes flow, we measure two quantities; namely the inclination angle θ obtained from the fitted ellipsoid, and the average tank-treading frequency (or average angular velocity) $\bar{\omega}$ obtained from

$$\bar{\omega} = \frac{\sum_{i=1}^{N_\phi} \sum_{j=1}^{N_\theta} \frac{|\mathbf{r}_{ij} \times \mathbf{V}_{ij}|}{|\mathbf{r}_{ij}|^2} dA_{ij}^k}{\sum_{i=1}^{N_\phi} \sum_{j=1}^{N_\theta} dA_{ij}^k}, \tag{34}$$

where the position vector of the Lagrangian marker \mathbf{r}_{ij} and its velocity \mathbf{V}_{ij} (interpolated from fluid velocity) both are projected onto the xz -plane. The markers with $|\mathbf{r}_{ij}| < 10^{-3}$ are excluded to avoid the computational overflow. The temporal evolution of these quantities for various ν is drawn in Fig. 5(a, b). As shown, all the quantities tend to be steady after $t = 5$. This implies that all the vesicles tested here undergo the steady tank-treading motion as illustrated in Fig. 4. The relative

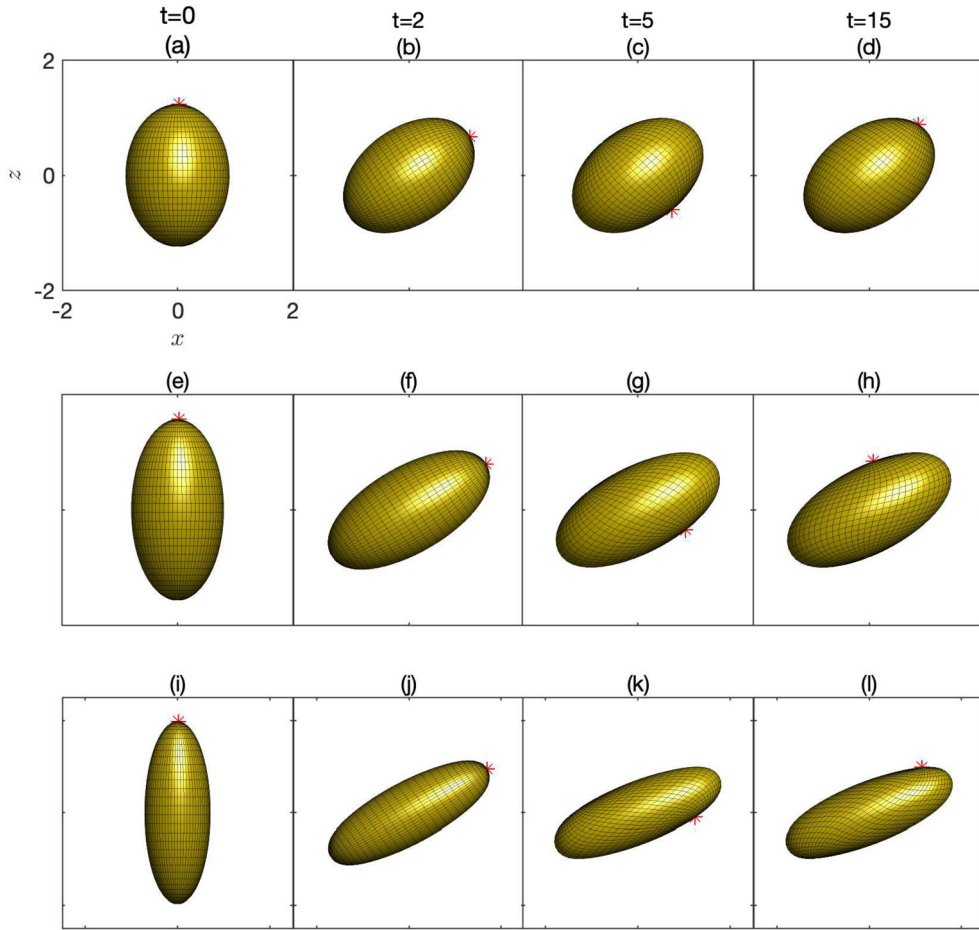


Fig. 4. Under shear flow, the snapshots of tank-treading motion of prolate vesicle whose reduced volume is (a-d) $\nu = 0.975$; (e-h) $\nu = 0.9$; (i-l) $\nu = 0.8$. The parameters are fixed by $Re = 10^{-3}$, $Ca = 2.5$, and $\lambda = 1$.

errors of the local and total surface area in terms of time are also plotted in Fig. 5(c, d), respectively. (Note that the error of $A(t)$ in the figure (d) is not an absolute value to see the increment/decrement of total surface area.) Although the maximum relative error of local surface area fluctuates a little particularly for small ν , it stays below 0.01 up to time $t = 15$. Despite the presence of fluctuations of dA , the relative errors of total surface area A tend to be almost constant for all ν tested here. This confirms that our present penalty approach enforcing the local interfacial incompressibility works well as a feedback mechanism to conserve the local surface area.

For comparison purpose, in Fig. 6, the steady-state results observed in Fig. 5(a, b) are plotted with those obtained in theory [17,22], experiment [46], and simulations [22,47,31]. In Fig. 6(a), the stationary inclination angle in terms of ν agrees well with other results, in particular better than that obtained by IB method using triangulated interface representation for vesicle [31]. On the other hand, in Fig. 6(b), the average tank-treading frequency deviates somewhat from other results. In many literatures on vesicle dynamics, it is common to employ the triangulation in approximating the vesicle interface and the formulas with equal weights in computing $\bar{\omega}$. So, we attribute the underestimated values of $\bar{\omega}$ to the usage of both spherical harmonic representation and different formula (34) with areal weights. Fortunately, as ν decreases, $\bar{\omega}$ gets closer to the theoretical prediction.

Before closing this subsection, we study the effect of the bending capillary number on vesicle deformation. In Fig. 7, the steady tank-treading motions of vesicle for $\nu = 0.975, 0.9, 0.8$ and $Ca = 0.25, 2.5, 25$ are depicted. For large $\nu = 0.975$, the vesicle shapes are almost identical to each other regardless of different Ca , while for moderate $\nu = 0.8$, the shapes deform significantly as Ca increases. This actually implies that the spherical harmonic representation for vesicle interface is suitably applicable to quasi-spherical vesicles for long time simulations.

4.5. Effect of viscosity contrast under shear flow

As a subsequent test, we consider the fluid has a viscosity contrast $\lambda > 1$. Under the same simulation setup used in the previous test, we study the effect of viscosity contrast on vesicle motion in shear flow. In Fig. 8, the inclination angle θ

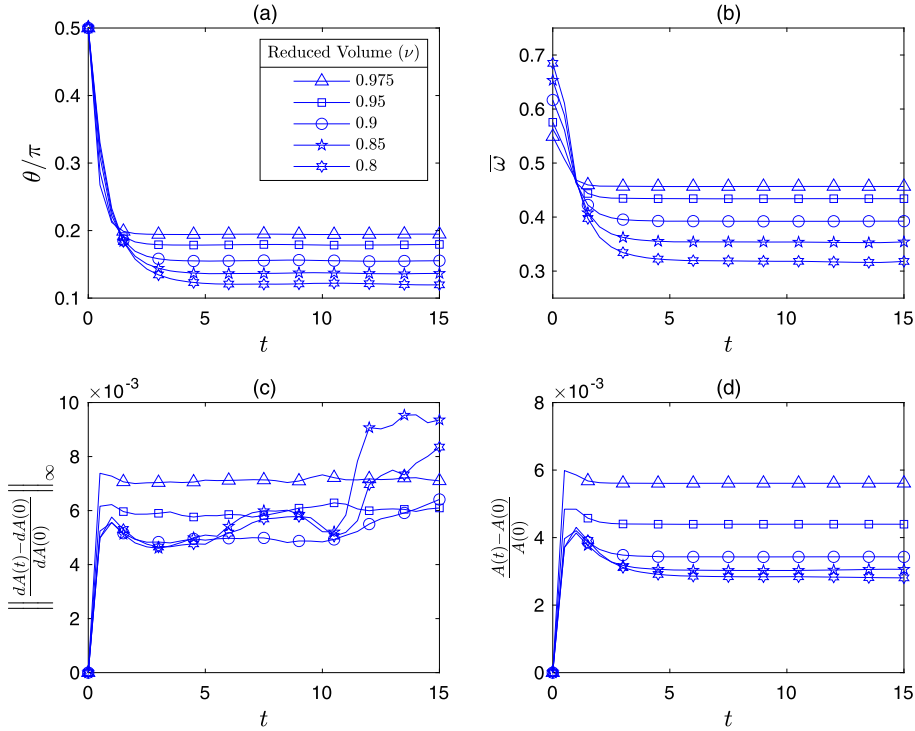


Fig. 5. The temporal evolution of (a) the inclination angle θ ; (b) the average angular velocity $\bar{\omega}$; (c) the maximum relative error of local surface area dA ; (d) the (non-absolute) relative error of total surface area A . The results of $\nu = 0.975, 0.9, 0.8$ correspond to Fig. 4.

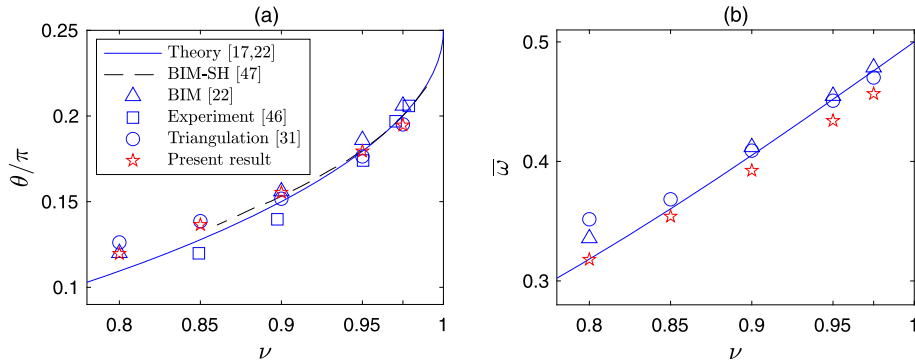


Fig. 6. The comparison of (a) the inclination angle θ ; (b) the average tank-treading frequency $\bar{\omega}$. The present results are the values at $t = 15$ taken from Fig. 5(a, b), respectively. There is no experimental result for $\bar{\omega}$.

for different $\lambda = 2.7, 5, 8$ is plotted in terms of the excess area defined by $\Sigma = 4\pi (\nu^{-2/3} - 1)$. For instance, three values of $\nu = 0.975, 0.95, 0.9$ correspond to the approximate excess areas $\Sigma = 0.21, 0.43, 0.91$, respectively. As shown, our results are compared with those obtained in experiment [46, Fig. 4], triangulation-based front-tracking method [45, Fig. 3], and boundary integral method using spherical harmonics (BIM-SH) [47, Fig. 6]. Note that the bending capillary number Ca defined in this paper is equivalent to $4Ca$ in other literature, due to the different definition of mean curvature H . We here defined H by the mean of two principal curvatures, whereas by the sum in literature. In the figure, our results for small λ and Σ are in good agreement with those obtained in the experiment and other simulations. As λ and Σ both increase, however, we observe some discrepancies from other results. This indicates that the usage of spherical harmonics in IB method is more proper to quasi-spherical vesicles, i.e., for large ν cases.

When the viscosity contrast λ is larger than a critical threshold, the vesicle undergoes tumbling motion. Fixing $\lambda = 20$, the temporal evolution of tumbling vesicles for $\nu = 0.975, 0.9, 0.8$ is illustrated in Fig. 9. For large ν , the deformation is small. As ν decreases, the vesicle deforms more, so the distortion of interfacial mesh becomes apparent and more severe. We emphasize that the filtering method for Lagrangian tangential velocity described in Subsection 3.3 indeed helps to

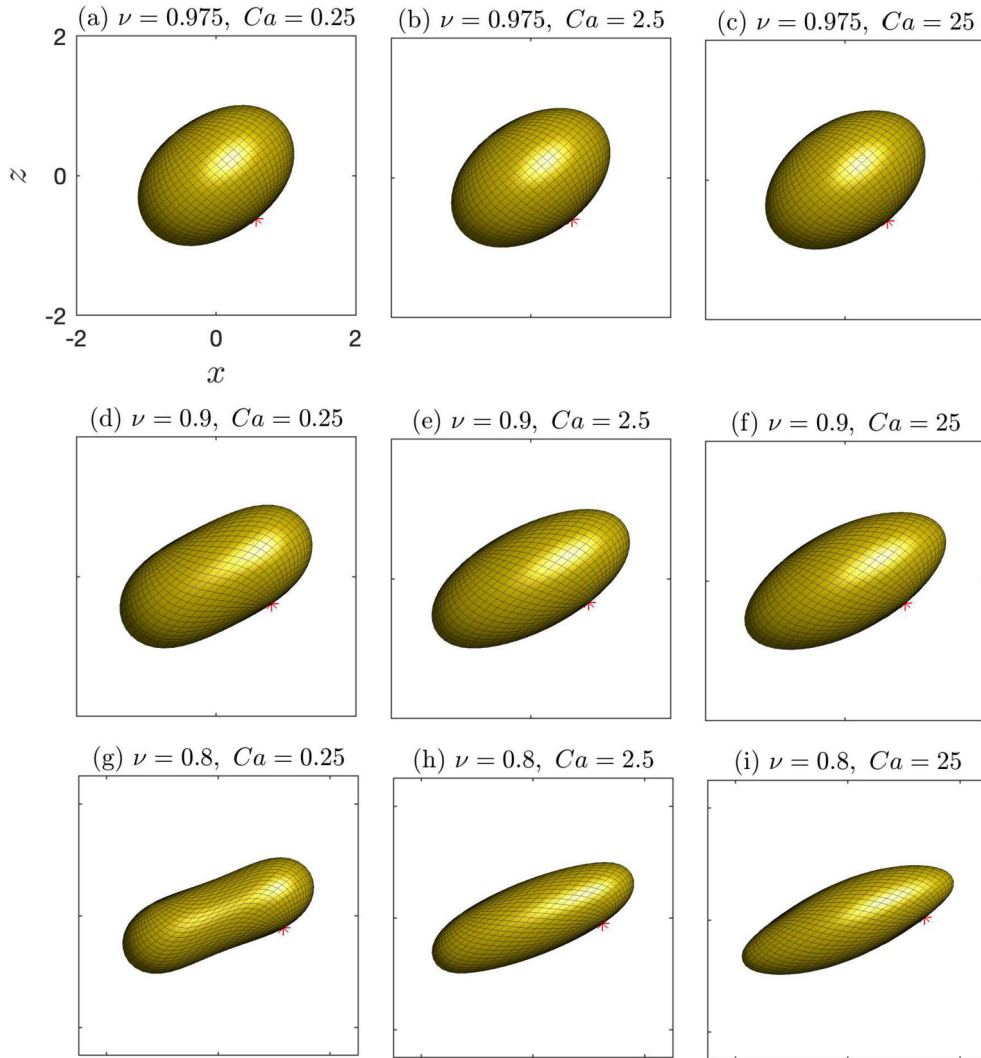


Fig. 7. Under shear flow, the steady tank-treading motion of prolate vesicle at time $t = 5$. Here ν and Ca denote the reduced volume and the bending capillary number, respectively. The flow is in Stokes regime with $Re = 10^{-3}$.

perform these stable simulations up to $t = 20$. Although omitted here, without the filtering, the simulation in shear flow breaks down at earlier time as observed in other tests.

4.6. Effect of Reynolds number under shear flow

Since our method can simulate Navier-Stokes flow, we now vary the Reynolds number Re to examine the inertia effect on the vesicle motion in shear flow. A prolate shape vesicle with $\nu = 0.9$ is used initially. The rest of the parameters are same as used in the previous subsection. The temporal evolution of the vesicle inclination angle for various Re is plotted in Fig. 10. Under Stokes regime $Re = 10^{-1}, 10^{-2}, 10^{-3}$, the results are almost identical, and the snapshots of vesicle motion are similar to the ones in Fig. 9(f-j) for the tumbling motion at $Re = 10^{-3}$. When $Re = 1$, the tumbling period is delayed, then as Re increases slightly more, the vesicle suddenly undergoes tank-treading motion and inhibits tumbling. Such tank-treading motion continues to appear for larger Re , and the steady value of θ increases gradually with increasing Re which is similar to 2D results of inertia effect described in [20, Fig. 8] and [29, Fig. 7]. In Fig. 11, two types of vesicle motion are compared at some chosen times. This apparently confirms that the tumbling vesicle may transit to tank-treading even at $Re = O(1)$. As a result, the inertia effect of fluid is not negligible in studying vesicle dynamics even in moderate Reynolds number flow.

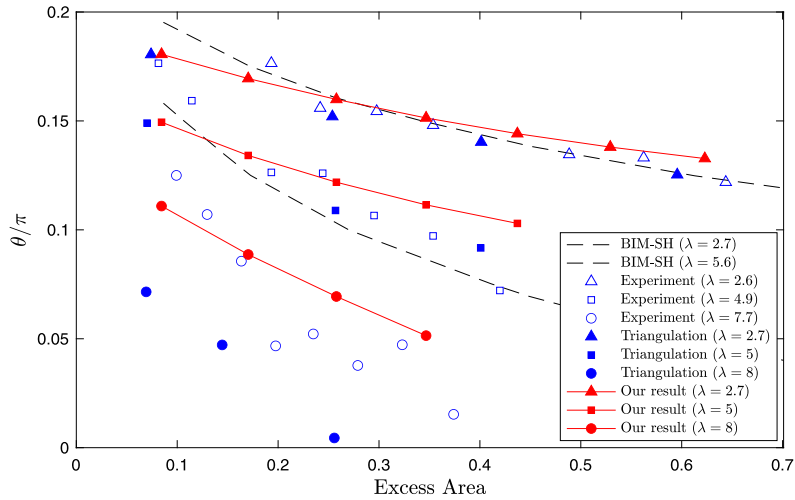


Fig. 8. In the presence of viscosity contrast $\lambda > 1$, the comparison of the inclination angle θ in terms of the excess area Σ defined by $4\pi(\nu^{-2/3} - 1)$, where ν is the reduced volume.

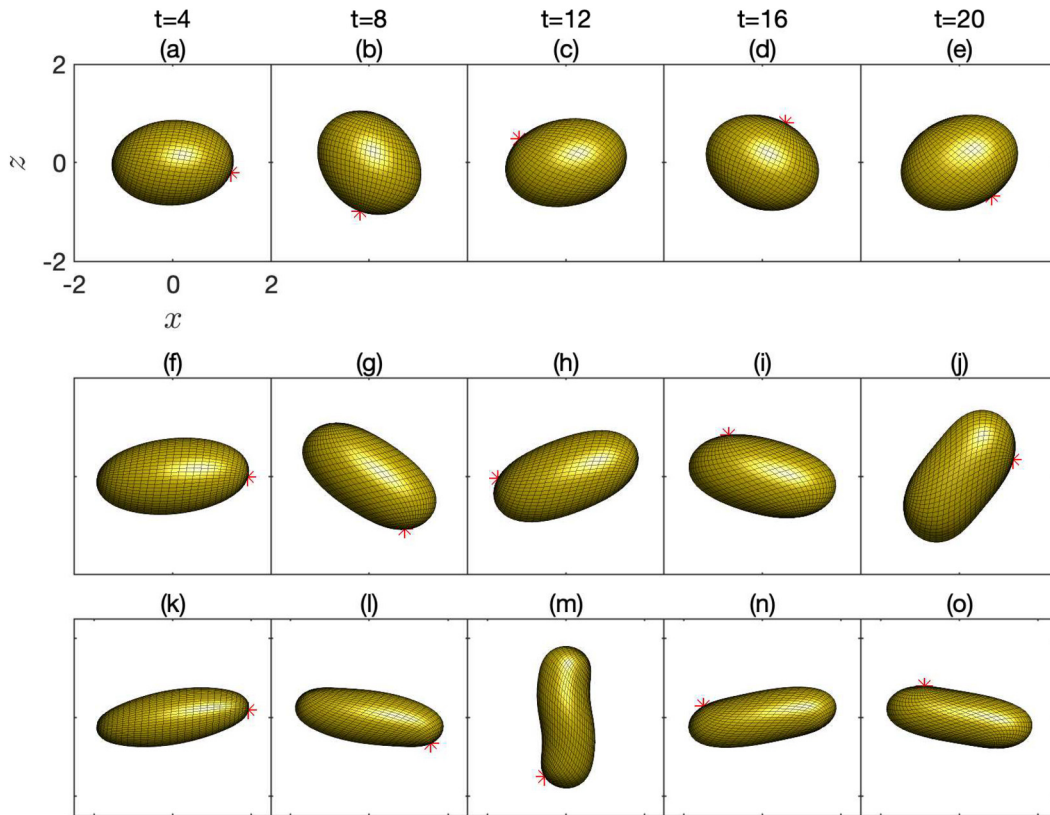


Fig. 9. The snapshots of tumbling motion for prolate vesicle with different reduced volume: (a-e) $\nu = 0.975$; (f-j) $\nu = 0.9$; (k-o) $\nu = 0.8$. The parameters are fixed by $Re = 10^{-3}$, $Ca = 2.5$, and $\lambda = 20$. This is the counterpart of Fig. 4 where the corresponding tank-treading motion is shown for $\lambda = 1$.

4.7. Vesicle motions in Poiseuille flow

So far, we have studied the motion of vesicle under quiescent and shear flow. As the last test, to demonstrate the applicability of our method, we study the vesicle dynamics under rectangular Poiseuille flow. For this, the computational domain is chosen as $[-10, 10] \times [-3, 3] \times [-3, 3]$ or $[-10, 10] \times [-3, 3] \times [-2.5, 2.5]$. The corresponding grid number is $(320, 96, 96)$ or $(320, 96, 80)$, respectively. Then the grid mesh width is $h = 6/N$ with $N = 96$. The time step size is chosen by $\Delta t = 1/(6N)$ and the total number of Lagrangian markers is $2N_\theta^2$ with $N_\theta = 64$. The dimensionless parameters are set by

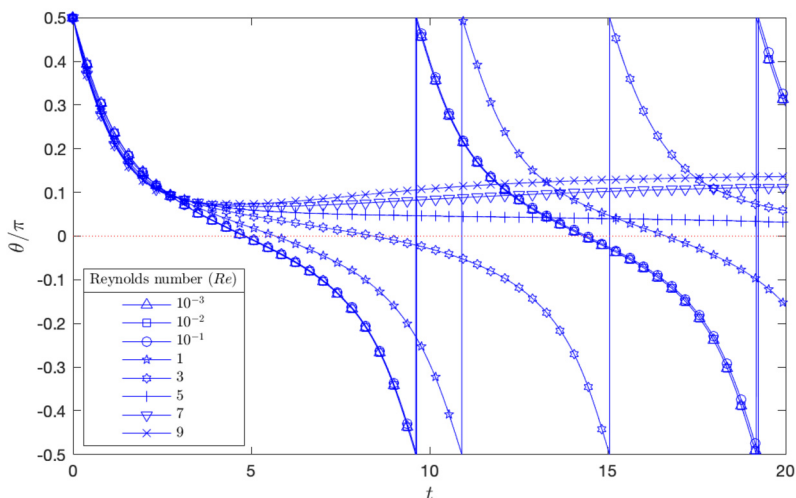


Fig. 10. The temporal evolution of inclination angle θ for various Re . The other parameters are fixed by $\nu = 0.9$, $Ca = 2.5$, and $\lambda = 20$.

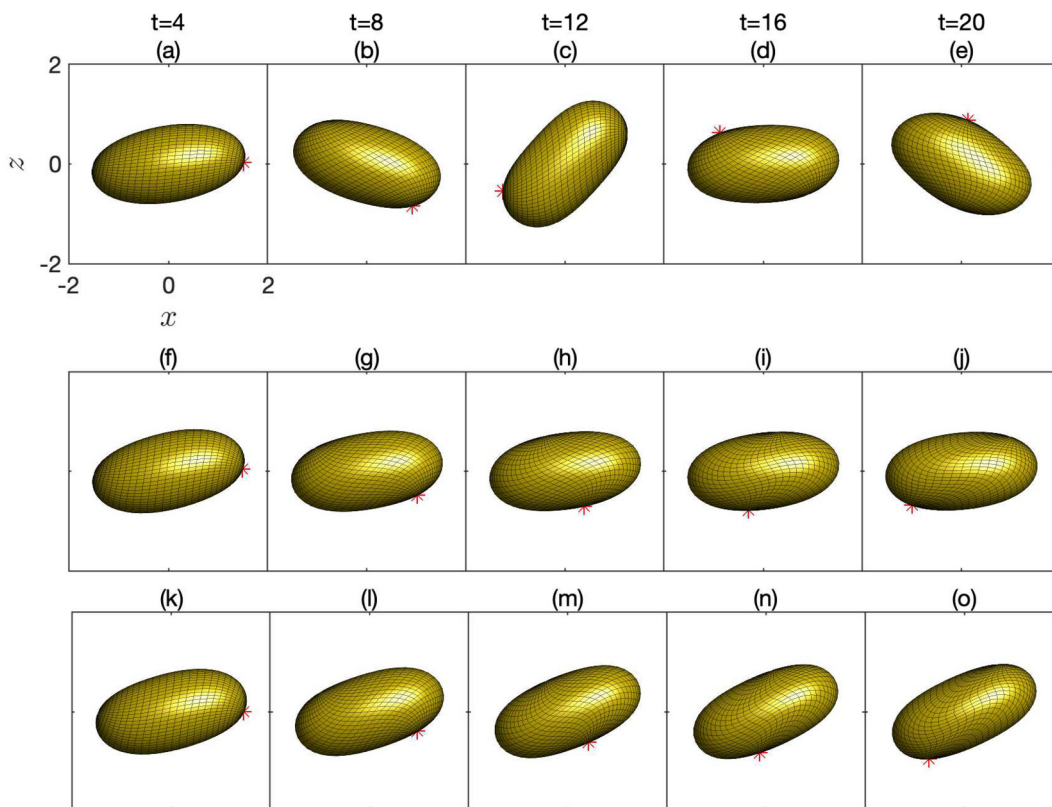


Fig. 11. The snapshots of prolate vesicle motion under shear flow with different Reynolds number: (a-e) $Re = 1$; (f-j) $Re = 5$; (k-o) $Re = 9$. The other parameters are fixed by $\nu = 0.9$, $Ca = 2.5$, and $\lambda = 20$. The corresponding inclinational angles are shown in Fig. 10.

$Re = 10^{-3}$, $Ca = 25$, $\lambda = 1$, $\sigma_0 = 12.5N$, and $c_v = 10^5$. We note that our definition of Ca is equal to one-fourth of that used in [6].

Let us consider a channel with rectangular cross-section, where its domain in the y -direction is defined by $-d \leq y \leq d$ (width) and that in the z -direction is by $-e \leq z \leq e$ (depth). After normalizing the exact solution of Poiseuille flow written in [43, Ch. 3-3.3], we use the following truncated series as the Dirichlet boundary condition of fluid velocity

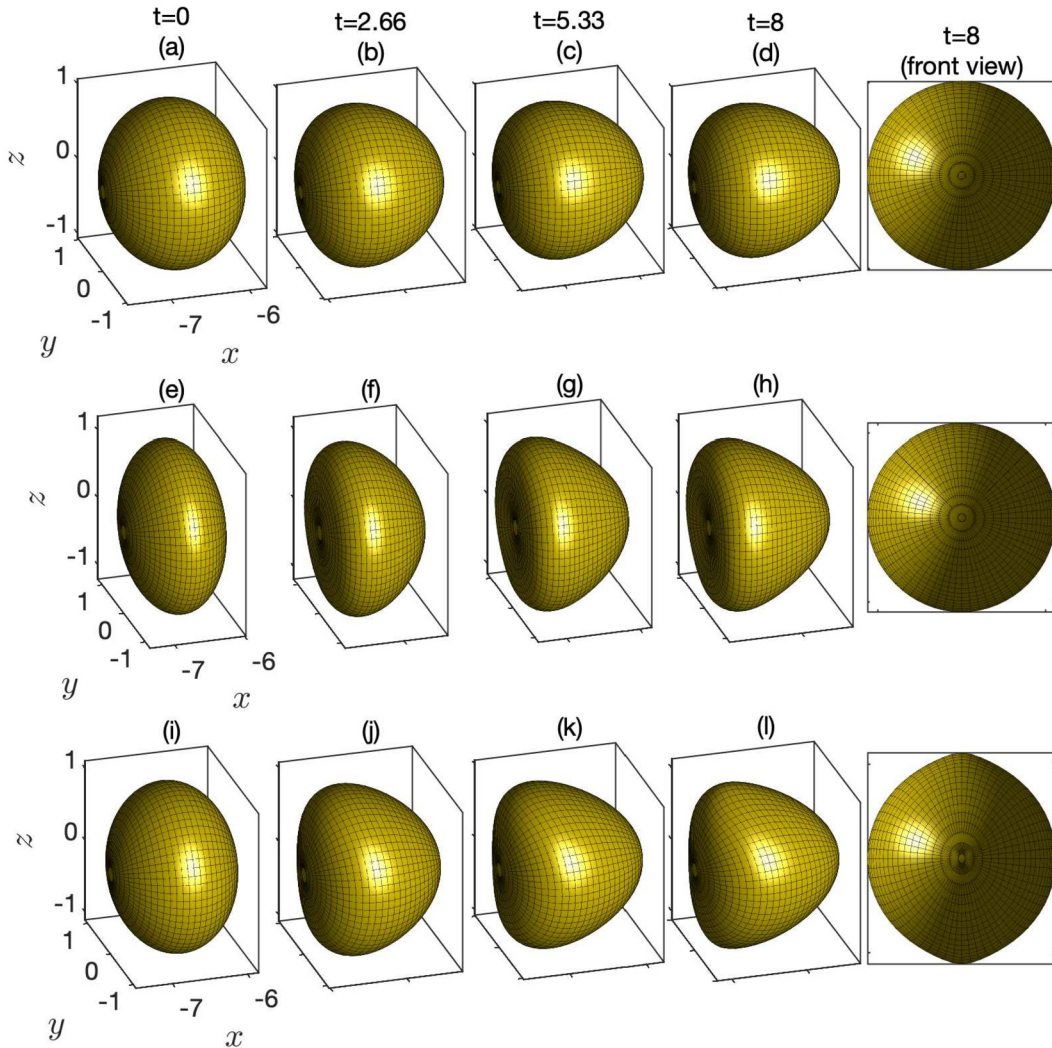


Fig. 12. Some snapshots of vesicle motion in Poiseuille flow, where (reduced volume ν , channel aspect ratio d/e) is (a-d) (0.99, 1); (e-h) (0.91, 1); (i-l) (0.973, 1.2). The vesicle deforms to a bullet shape in (a-d); a parachute shape in (e-h); a croissant shape in (i-l).

$$u(y, z) = \frac{1}{u_0} \sum_{i=1,3,5,\dots}^{199} \frac{(-1)^{(i-1)/2}}{i^3} \left[1 - \frac{\cosh\left(\frac{i\pi z}{2d}\right)}{\cosh\left(\frac{i\pi e}{2d}\right)} \right] \cos\left(\frac{i\pi y}{2d}\right), \tag{35}$$

$$v = 0, \quad w = 0, \tag{36}$$

where $u_0 = u(0, 0)$ in (35) is used to normalize the velocity. Due to $1/199^3 \approx 10^{-7}$, the truncation error will be very small.

We initially construct three configurations of ellipsoidal vesicle, whose aspect ratios are 3 : 3 : 2.5 ($\nu = 0.99$), 3 : 3 : 1.7 ($\nu = 0.91$), and 3 : 3 : 2.2 ($\nu = 0.973$). These are then rescaled to have the enclosed volume of $4\pi/3$. We put the first vesicle ($\nu = 0.99$) into the rectangular Poiseuille flow with $d/e = 1$ $[-10, 10] \times [-3, 3] \times [-3, 3]$, so the vesicle moves to the x -direction. As shown in Fig. 12(a-d), the vesicle deforms to a bullet shape, where the rear part is convex. For the second vesicle ($\nu = 0.91$) in the same simulation setup, the vesicle changes to a parachute shape in Fig. 12(e-h), where the rear part is now concave unlike the first case. This implies that large reduced volume close to one induces positive mean curvature of the rear, while the reduced volume smaller than a critical threshold induces negative mean curvature. Such observation agrees well with the experimental result obtained in [6, Fig. 4]. For the third vesicle ($\nu = 0.973$), to see the effect of the aspect ratio of the channel, we put the vesicle into the domain $[-10, 10] \times [-3, 3] \times [-2.5, 2.5]$ with aspect ratio $d/e = 1.2$. In Fig. 12(i-l), we observe that the vesicle deforms to a croissant shape as reported in the experiment [6]. As further emphasized in the paper, it is interesting to see that the croissant shape is relatively wider in the narrower direction of the channel. In the current test, the depth (z) of the rectangular channel is narrower than the width (y), but the resulting

shape of vesicle is wider in the z -direction. This verifies that our method can simulate vesicle dynamics in various flows properly.

5. Conclusion

For simulating quasi-spherical vesicles in unsteady Navier-Stokes flow, we have improved our prior 3D immersed boundary (IB) method using triangulation in nearly incompressible interface approach [31]. In this paper, four improvements are made; namely, the spherical harmonic representation of vesicle interface, the logarithmic form of approximate elastic tension, the divergence form of discrete elastic tension force, and the modified approach of nearly incompressible interface coupled with mesh control.

A major contribution is the usage of spherical harmonic expansion in approximating vesicle interface. By doing so, we are able to obtain high accuracy of the bending force, in particular the needed mean and Gaussian curvatures, and the surface Laplacian of mean curvature which is not feasible on triangulated surface as studied in [31]. The simultaneous imposition of fluid and interfacial incompressibilities is another challenging task in vesicle dynamics. To overcome this difficulty, we introduce an explicit logarithmic form of elastic tension mathematically consistent with the evolution equation of local surface area. With the approximate elastic tension known a priori, we find that the corresponding tension force in divergence form improves the overall numerical stability of vesicle motion. To demonstrate clearly, compelling numerical evidences are provided through the results of vesicle relaxation in quiescent flow. Although omitted here, the divergence form helps to improve the stability in dynamic flow as well. The discrete interface represented by spherical harmonic expansion inherently employs spherical coordinates. Unlike triangulated interface, such interfacial mesh often suffers from mesh distortion. In the present study, the vesicle in shear flow undergoes the tank-treading and tumbling motions, so we introduce a filtering technique to maintain the quality of interfacial mesh via spherical harmonic transform. All these new improvements are put together so that a numerical scheme for nearly incompressible vesicle coupled with mesh control in unsteady Navier-Stokes flow is developed. Furthermore, we verify the accuracy and applicability of present method through investigating the quantitative and qualitative results by varying the vesicle configuration and some dimensionless parameters associated with bending resistance, viscosity contrast, and inertia effect. Under rectangular Poiseuille flow, we also identify three types of vesicle shape, bullet, parachute, and croissant.

The smallest reduced volume used in this paper is about $\nu = 0.71$ shown in Fig. 3(a). Although not shown here, we were able to simulate a vesicle with the smaller $\nu = 0.6$ in a quiescent flow. However, the smaller ν indicates that the vesicle shape becomes longer or thinner as time evolves. So the local arclength ratio between the α and β axes or the maximum difference between the longest and shortest arclengths can be too large. For long-time simulations in dynamical flows, this surface mesh distortion gets worse and eventually leads to numerical instability. One can avoid such problem by adopting much smaller time step size, which is usually not preferable. Instead, a better adaptive mesh refinement algorithm for spherical coordinates will help to suppress such instability, and we shall leave it for future work.

CRedit authorship contribution statement

Ming-Chih Lai: Conceptualization, Supervision, Validation, Writing – review & editing. **Yunchang Seol:** Investigation, Methodology, Software, Writing – original draft.

Declaration of competing interest

The authors declare that they have no known competing financial interests or personal relationships that could have appeared to influence the work reported in this paper.

Acknowledgement

The work of M.-C. Lai was supported in part by Ministry of Science and Technology of Taiwan under research grant MOST-107-2115-M-009-016-MY3. The work of Y. Seol was supported by the basic science research program through the National Research Foundation of Korea (NRF) funded by the Korea government (NRF-2020R1A4A1018190).

References

- [1] S. Aland, S. Egerer, J. Lowengrub, A. Voigt, Diffuse interface models of locally inextensible vesicles in a viscous fluid, *J. Comput. Phys.* 277 (2014) 32–47.
- [2] J.W. Barrett, H. Garcke, R. Nürnberg, Numerical computations of the dynamics of fluidic membranes and vesicles, *Phys. Rev. E* 92 (2015) 052704.
- [3] T. Biben, K. Kassner, C. Misbah, Phase-field approach to three-dimensional vesicle dynamics, *Phys. Rev. E* 72 (2005) 041921.
- [4] G. Boedec, M. Leonetti, M. Jaeger, 3D vesicle dynamics simulations with a linearly triangulated surface, *J. Comput. Phys.* 230 (2011) 1020–1034.
- [5] K.-Y. Chen, K.-A. Feng, Y. Kim, M.-C. Lai, A note on pressure accuracy in immersed boundary method for Stokes flow, *J. Comput. Phys.* 230 (2011) 4377–4383.
- [6] G. Couplier, A. Farutin, C. Minetti, T. Podgorski, C. Misbah, Shape diagram of vesicles in Poiseuille flow, *Phys. Rev. Lett.* 108 (2012) 178106.
- [7] Q. Du, C. Liu, X. Wang, A phase field approach in the numerical study of the elastic bending energy for vesicle membranes, *J. Comput. Phys.* 198 (2004) 450–468.
- [8] B.S. Duncan, A.J. Olson, Approximation and characterization of molecular surfaces, *Biopolymers* 33 (1993) 219–229.

- [9] A. Farutin, T. Biben, C. Misbah, 3D numerical simulations of vesicle and inextensible capsule dynamics, *J. Comput. Phys.* 275 (2014) 539–568.
- [10] A. Fischer, A. Franco, T. Oberholzer, Giant vesicles as microreactors for enzymatic mRNA synthesis, *ChemBioChem* 3 (2002) 409–417.
- [11] A. Guckenberger, M.P. Schraml, P.G. Chen, M. Leonetti, S. Gekle, On the bending algorithms for soft objects in flows, *Comput. Phys. Commun.* 207 (2016) 1–23.
- [12] J.L. Guermond, P. Mineev, J. Shen, An overview of projection methods for incompressible flows, *Comput. Methods Appl. Mech. Eng.* 195 (2006) 6011–6045.
- [13] I. Halliday, S.V. Lishchuk, T.J. Spencer, G. Pontrelli, C.M. Care, Multiple-component lattice Boltzmann equation for fluid-filled vesicles in flow, *Phys. Rev. E* 87 (2013) 023307.
- [14] F.H. Harlow, J.E. Welsh, Numerical calculation of time-dependent viscous incompressible flow of fluid with a free surface, *Phys. Fluids* 8 (1965) 2181–2189.
- [15] W. Helfrich, Elastic properties of lipid bilayers: theory and possible experiments, *Z. Naturforsch., C* 28 (1973) 693–703.
- [16] B. Kaoui, J. Harting, Two-dimensional lattice Boltzmann simulations of vesicles with viscosity contrast, *Rheol. Acta* 55 (2016) 465–475.
- [17] S.R. Keller, R. Skalak, Motion of a tank-treading ellipsoidal particle in a shear flow, *J. Fluid Mech.* 120 (1982) 27–47.
- [18] K. Khairy, J. Howard, Minimum-energy vesicle and cell shapes calculated using spherical harmonics parameterization, *Soft Matter* 7 (2011) 2138–2143.
- [19] Y. Kim, M.-C. Lai, Simulating the dynamics of inextensible vesicles by the penalty immersed boundary method, *J. Comput. Phys.* 229 (2010) 4840–4853.
- [20] Y. Kim, M.-C. Lai, Numerical study of viscosity and inertial effects on tank-treading and tumbling motions of vesicles under shear flow, *Phys. Rev. E* 86 (2012) 066321.
- [21] E.M. Kolahdouz, D. Salac, Electrohydrodynamics of three-dimensional vesicles: a numerical approach, *SIAM J. Sci. Comput.* 37 (3) (2015) B473–B494.
- [22] M. Kraus, W. Wintz, U. Seifert, R. Lipowsky, Fluid vesicles in shear flow, *Phys. Rev. Lett.* 77 (1996) 3685–3688.
- [23] A. Laadhari, P. Saramito, C. Misbah, Computing the dynamics of biomembranes by combining conservative level set and adaptive finite element methods, *J. Comput. Phys.* 263 (2014) 328–352.
- [24] M.-C. Lai, Y. Seol, A short note on Navier-Stokes flows with an incompressible interface and its approximations, *Appl. Math. Lett.* 65 (2017) 1–6.
- [25] H. Noguchi, G. Gompper, Shape transitions of fluid vesicles and red blood cells in capillary flows, *Proc. Natl. Acad. Sci. USA* 102 (2005) 14159–14164.
- [26] K.C. Ong, M.-C. Lai, An immersed boundary projection method for simulating the inextensible vesicle dynamics, *J. Comput. Phys.* 408 (2020) 109277.
- [27] C.S. Peskin, The immersed boundary method, *Acta Numer.* 11 (2002) 479–517.
- [28] A.S. Popel, P.C. Johnson, Microcirculation and hemorheology, *Annu. Rev. Fluid Mech.* 37 (2005) 43–69.
- [29] D. Salac, M.J. Miksis, Reynolds number effects on lipid vesicles, *J. Fluid Mech.* 711 (2012) 122–146.
- [30] <https://www2.cisl.ucar.edu/resources/legacy/spherepack>.
- [31] Y. Seol, W.-F. Hu, Y. Kim, M.-C. Lai, An immersed boundary method for simulating vesicle dynamics in three dimensions, *J. Comput. Phys.* 322 (2016) 125–141.
- [32] S. Sofou, Surface-active liposomes for targeted cancer therapy, *Nanomedicine* 2 (2007) 711–724.
- [33] C. Sorgentone, A.-K. Tornberg, A highly accurate boundary integral equation method for surfactant-laden drops in 3D, *J. Comput. Phys.* 360 (2018) 167–191.
- [34] P.N. Swarztrauber, On the spectral approximation of discrete scalar and vector functions on the sphere, *SIAM J. Sci. Comput.* 16 (6) (1979) 934–949.
- [35] P.N. Swarztrauber, The vector harmonic transform method for solving partial differential equations in spherical geometry, *Mon. Weather Rev.* 121 (1993) 3415–3437.
- [36] P.N. Swarztrauber, Spectral transform methods for solving the shallow water equations on the sphere, *Mon. Weather Rev.* 124 (1996) 730–744.
- [37] P.N. Swarztrauber, On computing the points and weights for Gauss-Legendre quadrature, *SIAM J. Sci. Comput.* 24 (3) (2002) 945–954.
- [38] S.O. Unverdi, G. Tryggvason, A front-tracking method for viscous, incompressible, multi-fluid flows, *J. Comput. Phys.* 100 (1992) 25–37.
- [39] S.K. Veerapaneni, D. Gueyffier, G. Biros, D. Zorin, A numerical method for simulating the dynamics of 3D axisymmetric vesicles suspended in viscous flows, *J. Comput. Phys.* 228 (2009) 7233–7249.
- [40] S.K. Veerapaneni, A. Rahimian, G. Biros, D. Zorin, A fast algorithm for simulating vesicle flows in three dimensions, *J. Comput. Phys.* 230 (2011) 5610–5634.
- [41] P.M. Vlahovska, R.S. Gracia, Dynamics of a viscous vesicle in linear flows, *Phys. Rev. E* 75 (2007) 016313.
- [42] J.L. Weiner, On a problem of Chen, Willmore et al., *Indiana Univ. Math. J.* 27 (1978) 19–35.
- [43] F.M. White, *Viscous Fluid Flow*, McGraw-Hill Science, 1991.
- [44] X. Yang, X. Zhang, Z. Li, G.-W. He, A smoothing technique for discrete delta functions with application to immersed boundary method in moving boundary simulations, *J. Comput. Phys.* 228 (2009) 7821–7836.
- [45] A. Yazdani, P. Bagchi, Three-dimensional numerical simulation of vesicle dynamics using a front-tracking method, *Phys. Rev. E* 85 (2012) 056308.
- [46] N.J. Zabusky, E. Segre, J. Deschamps, V. Kantsler, V. Steinberg, Dynamics of vesicles in shear and rotational flows: modal dynamics and phase diagram, *Phys. Fluids* 23 (2011) 041905.
- [47] H. Zhao, E.S.G. Shaqfeh, The dynamics of a vesicle in simple shear flow, *J. Fluid Mech.* 674 (2011) 578–604.